

Physical Conditions in the Narrow-Line Region of Markarian 3.

II. Photoionization Modeling Results¹

N.R. Collins², S.B. Kraemer², D.M. Crenshaw³, F.C. Bruhweiler² & M. Mélandez⁴

ABSTRACT

We have examined the physical conditions in the narrow-line region (NLR) of the Seyfert 2 galaxy Markarian 3, using long-slit spectra obtained with the *Hubble Space Telescope*/Space Telescope Imaging Spectrograph and photoionization models. We find three components of photoionized gas in the NLR. Two of these components, characterized by emission lines such as [Ne V] λ 3426 and [O III] λ 5007, lie within the envelope of the bi-conical region described in our previous kinematic study. A component of lower ionization gas, in which lines such as [O II] λ 3727 arise, is found to lie outside the bi-cone. Each of these components is irradiated by a power-law continuum which is attenuated by intervening gas, presumably closer to the central source. The radiation incident upon the low ionization gas, external to the bi-cone, is much more heavily absorbed. These absorbers are similar to the intrinsic UV and X-ray absorbers detected in many Seyfert 1 galaxies, which suggests that the collimation of the ionizing radiation occurs in a circumnuclear wind, rather than a thick, molecular torus. We estimate the mass for the observed NLR emitting gas to be $2 \times 10^6 M_{\odot}$. It is likely that Markarian 3 acquired this gas through an on-going interaction with the spiral galaxy UGC 3422.

Subject headings: galaxies: individual (Markarian 3) – galaxies: Seyfert – line: formation

¹Based on observations made with the NASA/ESA *Hubble Space Telescope*, obtained at the Space Telescope Science Institute, which is operated by the Association of Universities for Research in Astronomy, Inc., under NASA contract NAS 5-26555

²Institute for Astrophysics and Computational Sciences, Department of Physics, The Catholic University of America; and Astrophysics Science Division, Code 667, NASA Goddard Space Flight Center, Greenbelt, MD 20771; nicholas.collins@nasa.gov, steven.b.kraemer@nasa.gov, frederick.c.bruhweiler@nasa.gov

³Department of Physics and Astronomy, Georgia State University, Atlanta, GA 30303

⁴NASA Postdoctoral Program Fellow, Goddard Space Flight Center, Code 662, Greenbelt, MD 20771; marcio@milkyway.gsfc.nasa.gov

1. Introduction

Markarian 3, which is among the brightest Seyfert 2 galaxies, is classified as a Hubble-type SB0 galaxy (Adams 1977). Its systemic velocity is 4050 km s^{-1} ($z = 0.0135$) based on H I 21 cm emission (Tift & Cocke 1988), which yields a distance of 53 Mpc for $H_0=75 \text{ km s}^{-1} \text{ Mpc}^{-1}$. At this distance, $1''$ corresponds to 257 pc. Spectropolarimetry of Markarian 3 revealed broad permitted lines and non-stellar continuum emission (Schmidt & Miller 1985). These observations are among those cited as evidence for the “unified” model for Seyfert galaxies (Antonucci 1993), which posits that the central engine and broad emission-line region (BLR) are surrounded by a dense molecular torus. In this model, when we observe a Seyfert 2 galaxy our line-of-sight is occluded by the torus and the central region is hidden. The Seyfert 2 active nucleus and BLR may sometimes be detected via radiation scattered into our line of sight by free electrons in the narrow emission-line region (NLR). In principle, one can probe into the nature of the hidden active galactic nucleus via a detailed study of the NLR gas.

In our earlier paper (Collins et al. 2005, ; hereafter Paper I), we used *Hubble Space Telescope*/Space Telescope Imaging Spectrograph (*HST*/STIS) longslit low-resolution spectroscopy from 1150 \AA to $10,300 \text{ \AA}$ to study the physical conditions in the narrow-line NLR of Markarian 3 (we refer the reader to Paper I for a more extensive discussion of earlier studies of Markarian 3). Here, we summarize the main results of Paper I. We found that the extinction within Markarian 3 along the line-of-sight to the NLR is best characterized by a Large Magellanic Cloud (LMC) type extinction curve (Koornneef & Code 1981). There is an extinction gradient increasing from West to East along the STIS slit (at position angle 71° measured East from North) in both line and continuum emission. We interpreted this gradient as evidence that the host galaxy disk is tilted towards the observer in the east. From emission-line diagnostics we argued that the NLR is photoionized by the hidden active galactic nucleus (AGN) continuum and that the density of the NLR gas decreases with increasing distance from the center. We modeled the observed continuum as a combination of reddened host galaxy light from an old stellar population, reddened H^+ and He^{+2} recombination continua, and scattered light from the central engine with spectral index $\alpha=1$ ($L_\nu \propto \nu^{-\alpha}$). The host galaxy to scattered-light ratio was estimated to be 3:1 at 8125 \AA in a $0''.1 \times 1''.8$ aperture. We fitted the intrinsic ionizing continuum with a two-component power-law of the form $L_\nu \propto \nu^{-\alpha}$, where $\alpha=2$ for $13.6 \text{ eV} < E < 0.2 \text{ keV}$ and $\alpha=1$ for $0.2 \text{ keV} < E < 50 \text{ keV}$. Based on this analysis, we estimated that the amount of intrinsic non-ionizing UV continuum scattered into our line-of-sight is 0.04%.

Kraemer & Harrington (1986) analyzed a combination of *International Ultraviolet Explorer* and ground-based spectroscopic observations of the Markarian 3 NLR, from ultraviolet

to infrared wavelengths. Based on this analysis, they found evidence for three components of emission-line gas. A single component would be insufficient to reproduce all the observed emission lines which arise from ionic species with ionization potentials up to 100 eV. Two of their model components included internal dust. The third component, which was the highest in ionization and density and closest to the central source, was assumed to be dust-free. Dust emission signatures are evident in the infrared continuum at $\lambda \sim 10\mu\text{m}$ (Neugebauer et al. 1976; Rieke 1978; Weedman et al. 2005). Kraemer & Harrington (1986) argued that these arose from hot dust within the two lower-density components. Since dust suppresses resonance line emission with large optical depths and the presence of dust requires depletion of C and Mg from the gas phase, they included the dust-free component to match the observed Ly α λ 1216, C IV $\lambda\lambda$ 1548,1551 and Mg II $\lambda\lambda$ 2796,2803 emission. In this study, we expand on these results through a photoionization modeling analysis of the STIS long-slit spectra presented in Paper I. This analysis has enabled us to determine the physical conditions as a function of radial distance, constrain the energetics of the central source, and develop new insight into the relationship between the structure of the NLR and the conditions in the unresolved circumnuclear region.

2. Observations and Analysis

The details of the observations and data reduction are described in Paper I. To summarize, *HST*/STIS longslit spectra were obtained on 2000 August 22 in all four low-resolution modes (G140L, G230L, G430L, and G750L) providing wavelength coverage from 1150 Å to 10,300 Å. The $52'' \times 0''.1$ slit was used for all spectral modes. The slit was oriented to position-angle 71° East of North to match the inner portion of the elongated reverse-“S” shaped feature in the brightest part of the central NLR (see Figure 1 in Paper I). We made seven discrete measurements of each emission line in the spatial direction. Individual spectra were extracted by summing array rows in selected bins in the spatial direction. The bin sizes were selected to extract spectral information for individual clouds and to achieve a signal-to-noise ratio greater than 5 for the He II λ 1640/ λ 4686 measurement: as discussed below, this ratio was used to determine the extinction along the line-of-sight to the NLR. The bin sizes range from 0.2-0.3 arcseconds, or 52-77 pc, using the adopted distance scale described in §1. In some measurement bins there are two kinematic components and/or two different lines are blended together. For those cases we used parameters (kinematic component velocity and velocity dispersion) derived from the [O III] λ 5007 line in the same bin as a template to separate the individual components.

We note here an error in the identification of the central NLR bin, that bin containing

the AGN. In Paper I Figure 6 the AGN is in the bin to the east of the bin indicated by the arrow (cf. Paper I Figure 1 which shows the correct identification). This error does not affect any of our conclusions in that paper. However, for the corrected plots vs. position (in arcseconds) along the slit all points would move towards the west. The bin labels in Paper I Tables 2 and 3 would be similarly corrected to the west as they are in §4.2 of this paper.

We corrected the observed flux measurements for both Galactic extinction along the line-of-sight to Markarian 3, and intrinsic extinction caused by dust within Markarian 3. The Galactic color-excess of $E(B - V) = 0.19$ was obtained from the dust map of Schlegel et al. (1998). We used the Savage & Mathis (1979) extinction curve to correct for Galactic extinction. We used the He II $\lambda 1640/\lambda 4686$ line ratio (Seaton 1978) to determine the extinction within Markarian 3 along the line-of-sight. This ratio has a longer wavelength baseline than the Balmer line ratio ($H\alpha \lambda 6563/H\beta \lambda 4861$) and therefore gives a better estimate of the reddening. It is also relatively insensitive to collisional excitation. As noted in Paper I, we found that the LMC curve of Koornneef & Code (1981) gave the best agreement for the He II $\lambda 1640/\lambda 4686$ and Balmer ratios with their theoretical values. Therefore, we used this curve and a screen geometry to de-redden the observed fluxes in this paper. The extinction corrected line fluxes relative to $H\beta \lambda 4861$ are listed in Table 3 of Paper I.

3. Photoionization Models

3.1. Preliminary Model Input Parameters

In this study we used version 95.06 of the photoionization modeling code CLOUDY (Ferland et al. 1998). As per convention, the photoionization models are parameterized in terms of the ionization parameter, U :

$$U = \frac{Q(H)}{4\pi r^2 n_H c} \quad (1)$$

where $Q(H)$ is the ionizing photon luminosity of the AGN in photons s^{-1} , r is the radial distance of the emitting cloud from the ionizing radiation source (the AGN in this case), n_H is the hydrogen number density in cm^{-3} and c is the speed of light. The photon luminosity and the spectral energy distribution are related by

$$Q(H) = \int_{\frac{13.6\text{eV}}{h}}^{\infty} \frac{L_\nu}{h\nu} d\nu \quad (2)$$

In Paper I, we parameterized the intrinsic ionizing continuum as follows: $L_\nu \propto \nu^{-\alpha}$, where $\alpha = 1$ for $h\nu < 13.6$ eV, $\alpha = 2$ for 13.6 eV $< h\nu < 200$ eV, and $\alpha = 1$ for $h\nu > 200$ eV, and

h is Planck’s constant. The high energy continuum slope is from the Turner et al. (1997) estimate (based on *ASCA* data) of the unabsorbed X-ray spectrum, with normalization such that the unabsorbed 2-10 keV integrated luminosity is 10^{44} ergs s^{-1} . This is consistent with the intrinsic luminosity derived by Matt et al. (2000) with *BeppoSAX* data and the prediction of Mélandez et al. (2008) extrapolated from a *Spitzer* [O IV] $\lambda 25.89 \mu\text{m}$ measurement. We truncated the continuum on the high energy end at 10^5 eV. Based on this parameterization, the intrinsic AGN continuum is extremely luminous, with $Q(H) \sim 2 \times 10^{55}$ photons s^{-1} .

We assume roughly solar chemical composition (e.g. Grevesse & Anders 1989) for all model components and absorbing screens (described in §3.4). The abundances relative to H by number are: He = 0.1, C = 3.4×10^{-4} , N = 1.2×10^{-4} , O = 6.8×10^{-4} , Ne = 1.1×10^{-4} , Mg = 3.3×10^{-5} , Si = 3.1×10^{-5} , S = 1.5×10^{-5} , Ar = 4.0×10^{-6} and Fe = 4.0×10^{-5} .

For model components that included dust (see §3.4) we used elemental depletions onto graphite and silicate grains that are half those of the standard Galactic interstellar medium (ISM) depletions. The Galactic ISM depletion fractions are 0.65 for C and 0.50 for O (Snow & Witt 1996); 0.90 for Al, 0.44 for S, 0.90 for Ca and 0.90 for Ni (Seab & Shull 1983). Snow & Witt (1996) list the ISM depletion for Fe, Mg and Si as 100%. We used a depletion of 95% for these elements. We do not account for nitrogen depletion, since nitrogen is deposited onto grains in ice mantles that would dissociate in the NLR. The gas phase abundances in the dusty model component are the nominal ISM values listed above multiplied by $0.5 \times (1 - f_{depletion})$ where $f_{depletion}$ represents the Galactic ISM depletion factor for the element of interest.

Our primary constraint on the models is that they reproduce the observed emission line fluxes. We required that the predicted fluxes of at least three-quarters of the twenty selected bright emission lines, each scaled to the predicted H β $\lambda 4861$ flux, match the data within a factor two. We also required that at least half of those lines within that gross limit match the data within $\pm 30\%$. It is possible to construct models in which the emission line fluxes match but the emitting clouds¹ may be unrealistically large. We implemented additional constraints to ensure that the models fit within our geometrical picture of the NLR and within the observational parameters of the *HST*/STIS spectra.

¹We refer to the regions over which we have summed the flux, then separated into individual kinematic components, as “clouds”.

3.2. Initial View of the NLR Structure

We initially assumed an NLR geometry based on the results of Ruiz et al. (2001). They studied the kinematics of the Markarian 3 NLR using [O III] $\lambda 5007$ measurements from a STIS/CCD slitless spectrum and from the same long-slit data that was presented in Paper I. Extracted spectra from several locations along the long-slit show evidence of two kinematic components: one is redshifted and the other is blueshifted in the rest-frame of Markarian 3. These components are interpreted as line-of-sight observations of radially outflowing gas on opposite sides of a NLR bi-cone. Their best-fit kinematic model assumes an NLR with an angular extent of $2''$ and inner and outer opening half-angles of 15° and 25° , respectively. The bi-cone is tilted toward the observer in the East and away from the observer in the West by 5° . The position angle of the the bi-cone is 70° East of North (Schmitt & Kinney 2000). The host galaxy disk major-axis position angle is 28° and the inclination of the disk is 33° (Schmitt & Kinney 2000). We converted the projected angular separation in arcseconds between the central engine and a measured kinematic component in the NLR into a radial distance using the bi-cone model opening angles and the $257 \text{ pc arcsecond}^{-1}$ scale factor from our estimated distance to Markarian 3. Redshifted kinematic components lie on the far side of the bi-cone and blueshifted components lie on the near side. For the central bin (hereafter angular position $0''0$) we assumed radial distances from the AGN for the redshifted and blueshifted components corresponding to one-quarter of the total $0''.3$ bin width.

We required that the model components fit within the intersection of the STIS slit, our measurement bins, and the bi-cone geometry. These three constraints correspond to the dispersion direction on the plane of the sky, the cross-dispersion direction on the plane of the sky, and the direction perpendicular to the sky plane, respectively. Each measurement bin may be considered as a small cell constrained, by the the projected slit width (26 pc), the measurement bin height along the slit, and the inner and outer bi-cone walls.

In this simple picture we envisioned a model component inside the measurement cell as a brick in which the illuminated face and the emitting face are the same. The model illuminated face is parallel to the cell face defined by the slit width and the lines between the inner and outer bi-cone walls at the slit edges. The model emitting face area was computed as the ratio a:b of (a) the observed $H\beta$ luminosity (ergs s^{-1}) of the measured kinematic component scaled by the fractional contribution of the model component to (b) the predicted $H\beta$ flux ($\text{ergs s}^{-1} \text{ cm}^{-2}$) for the model component. This emitting area must be on the order of cell face area.

We refer to the distance between the bi-cone walls as the “bin depth”. We calculate a “model component depth” by taking the ratio of the emitting area to the projected slit width in pc. It is unlikely that the bi-cone has a sharp cut-off. Kraemer, Schmitt, & Crenshaw

(2008) suggest that the NGC 4151 NLR does not have a sharp edge. Therefore, we allow the model component depth to be up to 1.5 times the “bin depth” at the center of the measurement bin. The height of the model component brick is given by the ratio of the model input parameters column density (in cm^{-2}) and volume number density (cm^{-3}). We required that this height be less than the measurement bin height along the STIS slit.

As a check that all model components fit within a measurement bin we computed the volume filling factor of each component. The volume filling factor is the ratio of the model component brick volume (emitting area multiplied by component height) to the measurement bin volume. We required that the sum of the volume filling factors of the model components within a bin be less than unity. We modified these geometrical constraints after analyzing the preliminary model results and reviewing the spectral image data (see §3.1).

In Paper I, we presented observational evidence that the n_H decreases with increasing distance from the AGN. For the modeling we did not assume a specific functional form for the radial dependence of model cloud number density. We simply required that a cloud must have the same or lower number density than the neighboring cloud in the direction of the AGN.

3.3. Evidence for Emission-Line Gas Outside the Bi-cone

As shown in Tables 2 and 3 in Paper I, each spectrum extracted along the slit shows a mix of strong emission lines from high and low ionization species, e.g., [Ne V] $\lambda 3426$ and [O II] $\lambda 3727$ (the unresolved blend of the 3726.0 \AA and 3728.8 \AA lines) emission, from the same kinematic component. This suggests that the observed emission along a line of sight to the Markarian 3 NLR may come from a combination of co-located clouds of different ionization states and optical thicknesses. Similar multi-component models have been used to model the NLR emission in the Sy 1 NGC 4151 (Kraemer et al. 2000) and the Sy 2 NGC 1068 (Kraemer & Crenshaw 2000a,b). The fact that the soft X-ray emission is roughly coincident with the optical emission-line gas in Markarian 3 (Sako et al. 2000) is further evidence for a heterogeneous NLR.

As noted in §3.1, the central source in Markarian 3 is quite luminous, which presents a problem for a simple, bi-conical model of the emission-line gas. For example, [O II] $\lambda 3727$ is predicted to be the strongest optical forbidden line for photoionized gas characterized by $U \lesssim 10^{-3}$ (Ferland & Netzer 1983). For that limit in U , our estimate for Q requires a density $n_H > 10^{5.7} \text{ cm}^{-3}$ for a cloud at a distance of 100 pc from the central source. However, the critical density for the $^2D_{3/2}$ level of O^+ , the upper level of the 3726 \AA line, is 1.6×10^4

cm^{-3} (Osterbrock 1989). Therefore, lines from low ionization species, originating from levels with low critical densities, will be collisionally suppressed since gas directly exposed to the ionization radiation in the inner NLR of Markarian 3 must have densities that significantly exceed the critical density.

The ionizing photon flux can be significantly reduced by an optically-thick screen. This effectively reduces the ionization state of the component, but the emission line flux will be weak due to the low emissivity of the gas. The emission line flux can be increased by adding more emitting material to the new model component. However, while matching the observed emission lines, we found that the emitting area of the gas can exceed the geometrical limits imposed by the bi-cone geometry and the STIS slit. This constraint can be met if the new low ionization state component lies further from the AGN than the other two model components. This gas would be outside the nominal bi-cone derived from the [O III] $\lambda 5007$ kinematic analysis (Ruiz et al. 2001). Interestingly, Kraemer & Crenshaw (2000a) similarly found that the emission near the NGC 1068 “Hot Spot” could be modeled by multiple components in which the lowest ionization state component is not co-planar with the others.

To test whether the lowest ionization state gas is more spatially extended than the high and medium ionization state gas we compared the [O III] $\lambda 4959$ emission with that of [O II] $\lambda 3727$ in the STIS spectral images (since these lines have similar fluxes). We extracted a subimage centered on the [O III] $\lambda 4959$ line from the G430L spectral image. The subimage size corresponds to a dispersion of 4000 km s^{-1} at 4959 \AA and $3''.0$ in the cross-dispersion direction. We derived an average continuum value from the line-fits described in Paper I and subtracted it from the subimage. We extracted a subimage centered on the [O II] $\lambda 3727$ line with a size corresponding to the same velocity dispersion as the [O III] $\lambda 4959$ line subimage. We subtracted the local continuum from this subimage. For direct comparison we used a linear interpolation algorithm to transform the [O II] $\lambda 3727$ line subimage so that each pixel would have the same velocity width as the [O III] $\lambda 4959$ line subimage.

We show the [O II] $\lambda 3727$ contours with [O III] $\lambda 4959$ contours overlaid in Figure 1. Note first the greater spatial extent of the [O II] $\lambda 3727$ line ($\sim 2''$) compared with that of the [O III] $\lambda 4959$ emission ($\sim 1''.5$). The [O II] $\lambda 3727$ emission is more extended by five spatial resolution elements in the West and 1 resolution element in the East. The [O II] $\lambda 3727$ line also shows greater extent in the velocity dispersion axis. On the redshifted side this line is more extended by at least a velocity resolution element, while on the blueshifted side it is extended by up to one resolution element. However, we do not interpret the greater extent in the dispersion direction as evidence that the lower ionization state gas has significantly different kinematic behavior than the high and medium state components comprising the nominal NLR bi-cone. Instead, this is most likely due to a difference in the spatial distri-

bution of these components within the slit in the dispersion direction. For example, the low ionization state gas may surround high and medium ionization state gas as has recently been suggested for NGC 4151 (Kraemer, Schmitt, & Crenshaw 2008). Therefore, the low ionization state gas may lie outside the nominal bi-cone configuration.

Another striking difference between the two spectral image contour maps is in the $0''.0$ measurement extraction bin. The [O III] $\lambda 4959$ line shows a strong blueshifted peak. The [O II] $\lambda 3727$ line shows no corresponding feature at this position. The observed flux in the [O III] $\lambda 4959$ line is greater than that in the [O II] $\lambda 3727$ line in this measurement bin (cf. Table 2 in Paper I). This contrast in line morphology may also be due to the more extended structure of the low ionization state gas.

We compared the [O III] $\lambda 4959$ spectral image morphology to that of [Ne V] $\lambda 3426$ to determine whether there might be evidence for spatial differences between high and medium ionization emission-line gas. The contours for those lines shown in Figure 2 show general correspondence for the major inner contour concentrations, although the centroids of the concentrations are slightly offset. The outer contours of both lines on average span the same range in the dispersion direction. In the spatial direction the 15% contours for [Ne V] $\lambda 3426$ do not extend past $0''.4$ east while those for [O III] $\lambda 4959$ reach $0''.6$ east. This may indicate that there is less high ionization state gas this far east along the STIS slit (see the discussion below in §4.2). We find no evidence for spatial separation between the high and medium ionization state gas from this data set. Hence, such components could be co-located within the bi-cone walls.

Although the [O II] $\lambda 3727$ and [O III] $\lambda 4959$ lines show different spatial morphologies, we found the same number of kinematic components in each measurement bin for the [O II] $\lambda 3727$ profiles as we did for the [O III] $\lambda 5007$ line. The kinematic components in both lines show the same sign relative to the Markarian 3 systemic velocity, i.e., blueshifted components in [O III] $\lambda 5007$ are blueshifted in [O II] $\lambda 3727$. Redshifted components in the two lines are likewise matched. The [O II] $\lambda 3727$ emitting kinematic components may have slightly different velocities and velocity dispersions than the [O III] $\lambda 5007$ emitting components. However, these differences cannot be distinguished from this data set better than the velocity resolution of ~ 316 km/sec at these wavelengths. Therefore, we maintain the use of the [O III] $\lambda 5007$ line kinematic parameters as templates for separating the blended kinematic components in other emission lines, including [O II] $\lambda 3727$, as described in §2.

3.4. Model Components

As we noted in the previous section the STIS spectrum of Markarian 3 NLR shows emission lines from ions spanning a wide range in ionization potential and from energy levels spanning a wide range in critical density for collisional de-excitation. Furthermore we provided evidence that the [O II] $\lambda 3727$ emission arises in a low ionization state component that is spatially distinct from the kinematically defined bi-cone. It is likely that the spectrum along any sight line to the NLR is produced by a heterogeneous ensemble of gas components (Kraemer & Harrington 1986) with different characteristic ionization parameters, hydrogen number densities and dust-to-gas ratios. In order to fit the observed line ratios and fluxes, we have included up to three model components for each radial position along the slit.

A high ionization state component (labeled “high”) produces most of the line emission observed from high ionization potential ionic species such as [Ne V] $\lambda 3426$ and [Fe VII] $\lambda 6087$. The presence of [Fe VII] emission is evidence that there is little depletion of iron onto dust grains within the high ionization gas, hence we assumed that this component is dust-free. We included a component with a lower ionization state (labeled “medium”) which would produce lines from lower ionization potential species such as C III] $\lambda 1909$, [Ne III] $\lambda 3869$ and [S III] $\lambda 9532$. The extinction-corrected Ly α /H β ratios (see Table 3 in Paper I) are generally lower than predicted for Case B recombination (Osterbrock 1989). This suggests that dust must be present in some component of the NLR gas. Therefore, following Kraemer & Harrington (1986), we assumed that dust was mixed with the emission-line gas in the “medium” component. However, the presence of strong C III] $\lambda 1909$ suggests that the dust/gas ratio is less than in the ISM of the Galaxy (e.g. Mathis, Rumpl, & Nordsieck (1977)). Hence, we selected a 50% depletion factor onto grains for “medium”. The third component (labeled “low”) is situated outside the nominal bi-cone. We did not include dust in the “low” component, since that decreased the emissivity of the gas. This decreased emissivity hampered our ability to reproduce the observed [O II] $\lambda 3727$ flux. However, we cannot rule out the presence of some dust within this component, albeit at less than the ISM dust/gas ratio.

The model components may be either matter bounded or radiation bounded. Binette, Wilson & Storck (1996) described matter bounded clouds as fully ionized and ionization bounded (or in this paper “radiation bounded”) clouds as partially ionized. In Paper I (§5.2) we inferred the presence of a mixture of matter and radiation bounded clouds in the Markarian 3 NLR. The component boundaries are model output parameters and are tabulated in §4.2.

Alexander et al. (1999) argued that the NLR emission-line ratios in the Seyfert 1 galaxy NGC 4151 indicated that the ionizing continuum was strongly absorbed above the He II Lyman limit. In a photoionization analysis of *HST*/STIS spectra of NGC 4151, Kraemer et al.

(2000) demonstrated that the intervening absorbers resembled the intrinsic absorption detected along the line-of-sight to the active nucleus. Since such an absorber will reduce the He^+ ionizing photon flux at $E \gtrsim 54.4$ eV, the $\text{He II } \lambda 4686/\text{H}\beta$ ratio will be lower than that predicted by photon-counting arguments. Based on previous studies (e.g. Kraemer et al. 2000), much of the NLR gas is matter bounded. This has the effect of increasing $\text{He II } \lambda 4686/\text{H}\beta$, since the H^+/H^0 transition zone may not be present. Therefore, in order to reproduce the observed $\text{He II } \lambda 4686/\text{H}\beta$, it is plausible that the intrinsic continuum is absorbed above the He II Lyman limit. Based on our preliminary modeling, we found that an absorber with column density $10^{20.4} \text{ cm}^{-2}$ and ionization parameter $10^{-1.5}$ yielded the best fits for these lines ratios (see Figure 3). Since the absorber is required for all of the observed components it must be well within the size of a detector spatial resolution element (26 pc).

As discussed above, the ionizing radiation to which the “low” component is exposed must be heavily filtered by gas close to the central source. In order to determine the characteristics of the screening material, we created a grid of screen models with a range in ionization parameter and in column density that absorb more ionizing photons than the screen for the “high” and “medium” ionization state components. The screens were sorted by transmitted photon flux. We selected the screen that appropriately reduced the ionizing continuum flux and yielded the best matches to the data for the lines $[\text{O II}] \lambda 3727$ and $[\text{N II}] \lambda \lambda 6548, 6583$ relative to $\text{H}\beta$ from the emitting cloud of interest. We used three types of absorbers for the low ionization state model components: (a) $U = 10^{-2.5}$ and $N_c = 10^{20.7} \text{ cm}^{-2}$, (b) $U = 10^{-1.5}$ and $N_c = 10^{21.6} \text{ cm}^{-2}$ and (c) $U = 10^{-3.0}$ and $N_c = 10^{21.9} \text{ cm}^{-2}$. The screened continua produced by each of these absorbers are shown in Figure 3. These screens absorb nearly all of emitted continuum from 13.6 eV to 200 eV. Most of the low ionization state clouds were screened by the $N_c = 10^{21.6} \text{ cm}^{-2}$ absorber. However, the eastern-most low ionization state cloud was screened by the $N_c = 10^{20.7} \text{ cm}^{-2}$ absorber while both the blueshifted and redshifted low ionization state clouds in the adjacent $0''.3$ measurement bin were screened by the $N_c = 10^{21.9} \text{ cm}^{-2}$ absorber.

Interestingly, these absorbers have physical parameters similar to the intrinsic absorbers detected in some Seyfert 1 galaxies. The low column density absorber that screens the nominal bi-cone gas is similar to the UV absorbers detected in NGC 5548 (Crenshaw et al. 2003). The screens for the low ionization state gas have column densities intermediate between those of the UV and X-ray absorbers in NGC 4151 (Kraemer et al. 2001).

4. Model Results

4.1. Revised View of the NLR Structure and Final Model Input Parameters

Based on our preliminary analysis, incorporating 1) the Ruiz et al. (2001) kinematics study and 2) the evidence for morphological differences in emission line spectral images from low and high ionization potential ionic species, we developed a revised model for the NLR structure, shown in Figure 4. Without higher spatial and spectral resolution observations of the [O II] $\lambda 3727$ line emission it is difficult to constrain the location of the low ionization components. As a guide for the models we located each low ionization component on the observer's sight line midway between the outer edge of the NLR bi-cone and a line that sweeps out two solid angles (East and West) of π steradians each when rotated around the bi-cone axis. This line is at a 38.7° angle with respect to the bi-cone axis. The ionizing continuum for the low ionization region (lighter grey shaded area in the figure) is more heavily absorbed than that illuminating the high and medium ionization regions. As noted, the screening is non-uniform for the low ionization state gas.

Although we have relaxed our constraint that all the emitting gas lie within the walls of the kinematically derived hollow bi-cone, we maintained the geometrical constraints for the high and low ionization state components. Those components produce nearly all of the [O III] $\lambda 5007$ emission on which the kinematically derived NLR structure is based. We loosely applied similar geometrical constraints on the low ionization state components using the inner and outer limits described above.

We list the final CLOUDY input parameters for all modeled components corresponding to our measured kinematic components in Table 1 of Appendix A. We did not include a dusty medium ionization state component for the central blue-shifted kinematic component, bin (0'0E (b), 0'3), since a two-component (high+low) model adequately reproduced the observed emission spectrum for this position in the NLR. In Figures 5 through 7 show the hydrogen number density (n_H) as a function of radial distance from the AGN for the high, medium and low ionization state components, respectively. Recall that we constrained the NLR density such that clouds further from the AGN have lower density than those closer to the AGN (see details in Paper I). However, we assumed no specific functional form for the cloud volume number density vs. position. For the high ionization parameter model components, the n_H decreases faster than r^{-2} in both the East and West along the STIS slit. The n_H within the dusty medium ionization state component falls off as approximately r^{-2} in the West. It is difficult to draw any conclusion about the radial dependence of the cloud hydrogen density in the east since there are only three data points for this component. The low ionization state component shows a density decrease in the West consistent with

r^{-2} . In the East, the data points follow the same functional form as those in the West out to $r \sim 150$ pc. For comparison, Kraemer et al. (2000) found the hydrogen density proportional to $\sim r^{-1.6}$ in the southwest along the STIS slit and $\sim r^{-1.7}$ in northeast for all model cloud components in the NGC 4151 NLR.

4.2. Fit to the Observations

In Tables 2 through 12 of Appendix A we list the line fluxes relative to $H\beta$ for each model component, the composite model, and for the observed data. The good agreement between the model emission line ratios and the observed emission line ratios indicates that our main assumptions about the NLR structure and intrinsic ionizing continuum were reasonable. Furthermore, the ionizing radiation emitted by the central source is sufficient to power the NLR, without additional ionization mechanisms such as shock-heating or starbursts. As suggested for other Seyfert galaxies (e.g., Kraemer et al. 2000; Kraemer & Crenshaw 2000a,b), multiple components with a range in ionization states comprise the NLR gas. Although the model predictions are consistent with at least some dust mixed in with the emission-line gas, the dust/gas ratio appears to be substantially less than that in the Galactic ISM. However, perhaps the most striking prediction of these models is that there is a strong contribution from a low ionization gas component which lies outside the nominal bi-cone structure. This provides new insight into the nature of the circumnuclear gas close to the AGN, which we will discuss in §5.

In Paper I we suggested that the continuum might be more heavily absorbed in the East than in the West based on the relative weakness of the high ionization potential emission lines [Ne V] $\lambda 3426$ and [Fe VII] $\lambda\lambda 5722, 6087$ on the eastern side of the NLR. However, we were able to fit these lines using a uniform screen in both directions for the high ionization state model component from which these observed lines would originate. Indeed the absorbing screen diagnostic ratio He II $\lambda 4686/H\beta$ shows no strong East/West asymmetry. In the models the effective ionization parameter and number density of the high ionization state component show no obvious asymmetry or trends with direction either. However, the high ionization state model components' emitting areas and masses are greater in the west than in the east. Perhaps the distribution of the high ionization state gas is asymmetric.

We list additional CLOUDY model output values, derived parameters and geometrical constraints in Table 13 of Appendix A. The emitting area, component depth, bin depth, component height and bin height were defined in §4.1. The ratios of component to bin depths for the high and medium ionization state model components meet the geometrical constraint (upper limit of 1.5). The component heights for these components are much less

than their corresponding measurement bin heights. Within each measurement bin the sum of the volume filling factors for the high and medium ionization components is less than unity. Therefore, it is unlikely that clouds at low radial distance from the AGN within the kinematically defined bi-cone shield clouds at higher radial distances.

Three of the low ionization components have component depth to bin depth ratios that exceed the 1.5 upper limit: ($0''.3\text{E}$, r, $0''.3$), ($-0''.7\text{W}$, r, $0''.3$) and ($-1''.0\text{W}$, r, $0''.3$). The second of these three has a filling factor near unity. It is possible this component may shield NLR gas located further from the AGN (measurement bin $-1''.0\text{W}$, r, $0''.3$), although we did not explore this possibility.

We created alternate models for the ($-0''.7\text{W}$, r, $0''.3$) component. In these models the number density ranged from $10^{2.0} \text{ cm}^{-3}$ to $10^{2.5} \text{ cm}^{-3}$ and the column density ranged from 10^{19} cm^{-3} to 10^{23} cm^{-3} . All models with good line fits violated one or another geometrical constraint. However, the geometry of the low ionization state gas outside the kinematically defined bi-cone is not well constrained. We conclude that more low-ionization gas is required to match the observed line ratios than would fit within the geometrical guidelines selected for the gas outside the nominal bi-cone. The extent of the low ionization gas along our lines of sight in the ($0''.3\text{E}$, r, $0''.3$), ($-0''.7\text{W}$, r, $0''.3$) and ($-1''.0\text{W}$, r, $0''.3$) measurement bins likely exceeds our geometrical guidelines for these components. It is possible that the lines of sight in the measurement bins ($0''.3\text{E}$, r, $0''.3$), ($-0''.7\text{W}$, r, $0''.3$) and ($-1''.0\text{W}$, r, $0''.3$) intersect foreground or background extended narrow-line region (ENLR) gas.

Based on the predicted electron temperatures (Table 13, Appendix A) and densities (Tables 2 through 12, Appendix A), it is apparent that the co-located “high” and “medium” components are not generally in pressure equilibrium. A more highly ionized medium, with a large volume filling factor (see §4.3), could confine one or both of these components. The apparent drop in density as a function of radial distance suggests that the UV/optical emission-line gas is not fully confined. The clouds may be part of an outflow originating close to the AGN and they may expand as they traverse the NLR (see Ruiz et al. 2001). However, it is likely that the clouds are at least partially confined, otherwise the density would decrease more rapidly with distance than our models predict.

Although the model predictions provide a good fit to the data, some discrepancies are evident. In several positions, notably $0''.3\text{E}$ (r), $0''.0\text{W}$ (r) and $-1''.0\text{W}$ (r), some combination of one, two or all three of the set of lines C III] $\lambda 1909$, C II] $\lambda 2326$ and [Ne IV] $\lambda 2424$ are underestimated. Recall that we used the LMC extinction curve of Koornneef & Code (1981) to correct our observations for intrinsic reddening within Markarian 3. This curve has a 2200\AA bump similar to that in the Galactic curve of Savage & Mathis (1979) on the long wavelength side of the feature. Toward shorter wavelengths the Koornneef & Code (1981)

extinction curve rises faster than the Savage & Mathis (1979) curve. This may be too steep for Markarian 3. If this is so, then we have over-corrected the line fluxes for extinction at these wavelengths, although the models do not consistently underestimate all three lines. Note that these three kinematic components are redshifted and therefore lie on the far side of the galaxy plane (at positions 0'3E (r) and 0'0W (r)) or in the galaxy plane (position -1'0W (r)) (see Figure 4) The corrected line fluxes at these positions may be more sensitive to uncertainties in the extinction correction than those at other positions. In particular, the positions 0'3E (r) and 0'0W (r) are in the region along the STIS slit that shows the greatest reddening (see Figure 8 in Paper I).

The model line fits for the position 0'5E (r) did not meet the criterion that half the model lines match the data within $\pm 30\%$. Generally the line fluxes in this component are underestimated by the model. If the column density of the “medium” ionization state model component is increased, improved fits to the data can be achieved; however, the emitting area will then violate our geometrical constraint for this measurement bin. This position is the most heavily reddened along the STIS slit and the UV lines shortward of 2400\AA are poorly fit. It is, thus, possible that the poor fits are due to over-correcting the measured line fluxes for extinction as discussed above. The underestimated He II $\lambda 4686$ model line flux may be an indication that the intrinsic absorption screen is too thick for this measurement position.

[S III] $\lambda 9532$ is under predicted in the bins 0'3E (r), 0'0E (b), 0'0W (r), -0'3W (b) and -0'W (r). Again this may be due to uncertainty in the shape of the extinction curve, and in this case the long base-line between the emitted line wavelength and the He II $\lambda 4686$ extinction reference line wavelength.

The predicted Ly α $\lambda 1216$ / H β $\lambda 4861$ ratio is low at positions 0'5E (r), 0'3E (r), 0'0W (r), -0'7W (r), -1'0W (r). As described above the extinction curve used to correct these observations (Koornneef & Code 1981) is steeper than the Galactic curve (Savage & Mathis 1979) at wavelengths shorter than 2200\AA . The actual extinction curve required for Markarian 3 may lie somewhere between these two.

Two positions, 0'3E (b) and 0'0E (b) show overestimated C IV $\lambda\lambda 1548, 1551$ flux. It is likely that the measurements for these lines at this position are poor, although this is not reflected in the $\pm 1\sigma$ error bars. Even though the flux ratio of the doublet is constrained (2:1), it is difficult to separate the four (2 doublet \times 2 kinematic component) lines. The Mg II flux is overestimated at position 0'0E (b). This is also likely due to poor separation of the blended doublet/kinematic component lines.

4.3. Model Comparison with X-Ray Data

We compared our model estimated X-ray lines with those observed by Sako et al. (2000) with *Chandra*/HETGS. They obtained a spectrum from $0.5 < E < 10$ keV (or $1 < \lambda < 24\text{\AA}$) through the $11'' \times 19''$ aperture. The aperture was oriented with the the cross-dispersion (longer) axis at position angle 90° to measure the flux from the entire NLR + ENLR. They detected eighteen resonance lines from the highly ionized H-like and He-like ionic species of O, Ne, Mg, Si and S. They also detected ten lines from Fe^{+20} through Fe^{+25} . They suggested that the X-ray emission-line gas was photoionized by the central source, thus it is useful to determine what, if any, contribution the UV/optical emission-line gas may have to the X-ray spectrum.

For each X-ray line we summed the fluxes computed by CLOUDY for all of our model components. To compare our predicted lines with the Sako et al. (2000) observations we must normalize the predictions using one of the lines in common. We assumed that the O^{+6} gas has the same distribution as the H^0 gas and used the O VII $\lambda 22.10$ line for normalization. We found a predicted flux of $\sim 10^{-14}$ ergs $\text{s}^{-1} \text{cm}^{-2}$. This is 30% of the observed flux for this line. The estimate is reasonable considering the difference in aperture sizes between STIS and HETGS. Our models predict significant emission only from the other oxygen lines observed: the predicted O VII $\lambda 21.60$ /O VII $\lambda 22.10$ ratio is 0.5 and the O VII $\lambda 21.81$ /O VII $\lambda 22.10$ ratio is 0.7. These ratios are somewhat higher than those reported in Sako et al. (2000). The physical conditions (e.g., optical depth and/or microturbulence) may be different in the the O VII emitting gas which lacks a strong UV/optical footprint. Also, since the models underestimate the observed flux for lines from the higher ionization potential ionic species, it is likely that the Markarian 3 NLR contains a yet higher ionization component, which produces little or no UV/optical emission-line flux. Given the low volume filling factors predicted for the UV/optical emission-line clouds (see Table 13 in Appendix A), and the weak attenuation of the ionizing continuum expected from the highly ionized gas, the X-ray emitters could be co-located with the “high” and “medium” components without any obvious affect. In this case, the volume filling factors for the X-ray emitters would far exceed those of the UV/optical knots, perhaps filling the bi-cone envelope.

5. Collimation of the Ionizing Radiation

Based on our models, the ionizing photon flux (and hence the gas ionization state) in the NLR decreases with increasing polar angle from the symmetry axis (nearly coincident with the sky plane). We suggest that the collimation of the ionizing radiation is not sharply defined by an opaque molecular torus as described in most unified model scenarios. Some

alternative mechanisms for collimation are a “torus atmosphere” or an accretion disk wind.

Evans et al. (1993) proposed a torus atmosphere model for NGC 4151 with a column density of order 10^{20} – 10^{21} cm^{-2} that absorbed X-rays but transmitted non-ionizing UV/optical radiation. Another model suggested by Evans et al. (1993) was a clumpy torus composed of clouds with a range of column densities and spatial distributions fortuitously arranged to allow transmission of the optical BLR and continuum emission while absorbing X-ray emission. Feldmeier et al. (1999) suggested that the intrinsic X-ray absorption detected in the Seyfert 1 galaxy Markarian 6 arose in a similar torus “atmosphere” of larger column density (10^{22} cm^{-2}). Interestingly, the narrow line region in each of these galaxies appears as a linear (as opposed to circular) feature in [O III] images (Schmitt & Kinney 1996; Schmitt et al. 2003). This morphological similarity with Markarian 3 suggests that these three NLRs share a common orientation.

In the hydromagnetic wind model of Konigl & Kartje (1994) an outflow is driven by the angular momentum lost by matter in the an accretion disk. The outflow is stratified such that density increases with distance from the nucleus. Electrons in the wind collimate the ionizing radiation which decreases with increasing polar angle. The gas close to the symmetry axis is highly ionized and the ionization state decreases with radius and polar angle.

The gas ionization state and density gradients are consistent with our picture of the circumnuclear gas in Markarian 3 developed from the analysis of the NLR emission. However, the ionizing radiation in our models is collimated through absorption by the circumnuclear gas instead of electron scattering. In the Konigl & Kartje (1994) model, the outer regions of the wind at high polar angle may contain dust. This dust may obscure the AGN as required by the unified model, but it is not considered a physically distinct opaque component such as the putative torus. We did not include dust in our model screens. The screens may lie within the dust sublimation radius (see Barvainis 1987) or they may be part of a wind that originates in a dust-free region. However, the physical conditions in the screening gas are not well constrained, so we cannot rule out the possibility that they contain dust. The main point is that the characteristics of the NLR are consistent with collimation of the ionizing radiation by ionized absorbers. Moreover, Markarian 3 may not be a unique case. Kraemer, Schmitt, & Crenshaw (2008) used [O III] and [O II] images obtained with *HST*/WFPC2 to map the ionization structure of the NLR in NGC 4151. They found that the ionization state of the of NLR, determined via the [O III]/[O II] ratio, dropped with increasing distance from the bicone axis, which is also consistent by a collimation of the ionization radiation by gas near the AGN.

6. Black Hole Mass, Accretion Rate and Outflow

Woo & Urry (2002) derived a black hole mass of $\approx 4.5 \times 10^8 M_\odot$ for Markarian 3 based on the M_{BH} - stellar velocity dispersion relationship. Using the bolometric luminosity of the model input continuum, 2×10^{45} ergs s^{-1} , we estimate that the AGN is radiating at $\sim 3.5\%$ of its Eddington limit. Kraemer et al. (2004) and Peterson et al. (2004) show evidence that many AGN radiate at $\sim 10\%$ of their Eddington limits.

We estimated the mass of the NLR gas using the volume and number density values for the clouds (see Table 13 in Appendix A), obtaining a value of $2 \times 10^6 M_\odot$ for the small portion of the NLR gas modeled in this study. By comparison, the NLR mass estimated for NGC 4151 from the photoionization models by Kraemer et al. (2000) is $\sim 4 \times 10^3 M_\odot$. This would correspond to $\sim 2 \times 10^4 M_\odot$ for the larger region sampled in Markarian 3. We estimate that we have sampled and modeled one-sixth of the hollow bi-cone volume with a 400 pc extent along the bi-cone axis. Assuming that the NLR mass distribution is roughly azimuthally symmetric, the total NLR mass along the 400 pc extent is $1.2 \times 10^7 M_\odot$. This is on the order of the mass of a late-type dwarf galaxy. For comparison, a typical late-type dwarf galaxy, such as the LMC, has an atomic hydrogen mass on the order of $10^8 M_\odot$ (Swaters et al. 2002; Staveley-Smith et al. 2003), while the dwarf elliptical galaxy NGC 205 has an H I mass of approximately $10^7 M_\odot$ (Welch et al. 1998). Noordermeer et al. (2005) found an H I bridge between Markarian 3 and UGC 3422, a type SAB(rs)b galaxy ~ 100 kpc to the north-west, in the Westerbork H I Spiral and Irregular Galaxy Survey (WHISP). This interaction is likely responsible for the large amount of emission-line gas inferred by the models and for triggering and sustaining the level of activity observed in Markarian 3.

The mass accretion rate, \dot{M} , is determined from the time derivative of Einstein's mass-energy equivalence relation and by assuming an efficiency, η , for the conversion of matter to light

$$\dot{M} = \frac{L}{\eta c^2} \quad (3)$$

Based on our estimated bolometric luminosity, and assuming $\eta = 0.1$, the accretion rate is $0.35 M_\odot \text{ yr}^{-1}$. This can be compared to the mass outflow rate that we derived using the cloud masses from the models, their distances from the AGN and their radial velocities relative to the AGN. We converted the line of sight cloud velocities to outflow velocities relative to the central source using the bi-cone model geometry. We obtain a mass outflow rate of $\sim 15 M_\odot \text{ yr}^{-1}$, or 42 times the accretion rate. This suggests that most of the infalling material is blown out before it can be accreted by the central source at the epoch of these observations. We find that the observed NLR outflow kinetic energy is 2×10^{55} ergs. The kinetic energy luminosity, 3×10^{42} ergs s^{-1} , is a small fraction of the bolometric luminosity.

Note that these estimates are lower limits for Markarian 3 since we modeled only a portion of the entire NLR.

7. Summary

We have examined the physical conditions in the NLR of the Seyfert 2 galaxy Markarian 3, using low-resolution, long-slit data obtained with *HST*/STIS (see Paper I) and photoionization models. The main results of our photoionization modeling analysis are as follows:

1. We have shown that the Markarian 3 NLR UV/optical emission spectrum can be modeled using photoionization as the sole excitation mechanism. The bulk of the emission-line gas lies within the envelope of the bi-conical region described in the kinematic model of Ruiz et al. (2001). We modeled the emission from this region using two components, labeled “high” and “medium” to describe their relative ionization state. We determined that the ionizing continuum incident upon this gas is best modeled as a broken power-law (see Paper I), filtered through a layer of intervening gas, closer to the AGN, that causes some attenuation above the He II Lyman limit.

2. There is a third component of emission (“low”) in which lines from levels with low critical densities from low ionization species, e.g. [O II] $\lambda 3727$, arise. In order for such a component to exist in the inner NLR of Markarian 3, it must be heavily shielded from the ionizing source, presumably by an optically thick intervening absorber. Given the nature of the shielding and the low emissivity of low density gas irradiating in such a manner, the “low” component must lie outside the nominal emission bi-cone. The different morphologies of the [O II] $\lambda 3727$ and [O III] $\lambda 4959$ lines are strong evidence for such a scenario.

3. The model parameters used to describe the intervening absorbers are similar to those derived from photoionization studies of intrinsic UV and X-ray absorbers in Seyfert 1 galaxies (Kraemer et al. 2001; Crenshaw et al. 2003). This suggests that intrinsic absorbers are responsible for the collimation of the ionizing continuum, rather than the thick molecular torus described by unified models (Antonucci 1993).

4. The volume filling of the emission-line components are generally small (<0.01), and the clouds of different ionization states are not in pressure equilibrium. The cloud densities decrease with radial distance, which suggests that they are not fully confined. Interestingly, our models predicted only 30% of the O VII $\lambda 22.10$ flux reported by Sako et al. (2000) and negligible fractions of the observed flux for higher ionization states. The additional soft X-ray emission-line gas could lie between the bi-cone walls, and may partially confine the UV/optical clouds.

5. We found that the ionizing radiation could be produced by accretion onto a black hole of $M_{BH} > 10^8 M_{\odot}$, with the system radiating at $< 10\%$ of its Eddington luminosity. The mass outflow rate exceeds the inferred accretion rate by a factor of ~ 40 .

6. The large amount of NLR gas is consistent with that in a dwarf elliptical galaxy. This mass, the high luminosity of the ionizing continuum and the dust structure (described in Paper I) may be indications of a recent merger or fueling event. Indeed, the H I map of Noordermeer et al. (2005) shows evidence of such an interaction with the neighboring spiral galaxy UGC 3422.

We thank Jane Turner for useful comments. We thank Gary Ferland for the use of CLOUDY and for helpful advice on running the models. We thank Henrique Schmitt for calling our attention to the H I map of Noordermeer et al. (2005). We thank the referee for constructive comments. Some of the data presented in this paper were obtained from the Multimission Archive at the Space Telescope Science Institute (MAST). STScI is operated by the Association of Universities for Research in Astronomy, Inc., under NASA contract NAS5-26555. Support for MAST for non-HST data is provided by the NASA Office of Space Science via grant NAG5-7584 and by other grants and contracts. This research has made use of NASA's Astrophysics Data System. This research has made use of the NASA/IPAC Extragalactic Database operated by the Jet Propulsion Laboratory, and NASA's Astrophysics Data System Bibliographic Services.

We acknowledge the financial support of NAG5-4103 and NAG5-13109.

Facilities: HST(STIS)

A. Tables

All tables should appear in this appendix.

REFERENCES

- Adams, T.F. 1977, ApJS, 33, 19
- Alexander, T., Sturm, E., Lutz, D., Sternberg, A., Netzer, H., & Genzel, R. 1999, ApJ, 512, 204
- Antonucci, R.R.J. 1993, ARA&A, 31, 473
- Barvainis, R. E. 1987, ApJ, 320, 537
- Binette, L., & Robinson, A. 1987, A&A, 177, 11
- Binette, L., Wilson, A. S. & Storchi-Bergmann, T. 1996, A&A, 312, 365
- Binney, J. & Merrifield, M. 1998 in “Galactic Astronomy” (Princeton University Press)
- Collins, N.R., Kraemer, S.B., Crenshaw, D.M., Ruiz, J., Deo, R. & Bruhweiler, F.C, ApJ, 619, 116 (Paper I)
- Crenshaw, D.M. et al. 2003, ApJ, 594, 116
- Evans, I.N., Tsvetanov, Z., Kriss, G.A., Ford, H.C., Caganoff, S. & Koratkar, A.P. 1993, ApJ, 417, 82
- Feldmeier, J.J., Brandt, W.N., Elvis, E., Fabian, A.C., Iwasawa, K. & Mathur, S. 1999, ApJ, 510, 167
- Ferland, G.J. & Netzer, H. 1983, ApJ, 264, 105
- Ferland, G. J., Korista, K.T., Verner, D.A., Ferguson, J.W., Kingdon, J.B. & Verner, E.M. 1998, PASP, 110, 761
- Grevasse, N. & Anders, E. 1989, “Cosmic Abundances of Matter”, AIP Conf. Proc. 183, ed. C.J. Waddington (New York: AIP)
- Konigl, A. & Kartje, J.F. 1994, ApJ, 434 446
- Koornneef, J. & Code, A.D. 1981, ApJ, 247, 860
- Kraemer, S.B. & Harrington, J.P. 1986, ApJ, 307, 478
- Kraemer, S.B., Crenshaw, D.M., Hutchings, J.B., Gull, T.R., Kaiser, M.E., Nelson, C.H. & Weistrop, D. 2000, ApJ, 531, 278

- Kraemer, S.B. & Crenshaw, D.M. 2000, ApJ, 532, 256
- Kraemer, S.B. & Crenshaw, D.M. 2000, ApJ, 544, 763
- Kraemer, S.B. et al. 2001, ApJ, 551, 671
- Kraemer, S.B., George, I.M., Crenshaw, D.M., & Gabel, J.R. 2001, ApJ, 607, 794
- Kraemer, S.B., Schmitt, H.R., & Crenshaw, D.M. 2008, ApJ, 679, 1128
- Mathis, J.S., Ruml, W., & Nordsieck, K.H. 1977, ApJ, 217, 425
- Matt, G., Fabian, A.C., Guainazzi, M., Iwasawa, K., Bassani, L. & Malaguti, G. 2000, MNRAS, 318, 173
- Mélandez, M., Kraemer, S. B., Armentrout, B. K., Deo, R. P., Crenshaw, D. M., Schmitt, H. R., Mushotzky, R. F., Tueller, J., Markwardt, C. B., Winter, L. 2008, ApJ, 682, 94
- Neugebauer, G., Becklin, J.B., Oke, J.B & Searle, L. 1976, ApJ, 205, 29
- Norrdermeer, E., van der Hulst, J.M., Sancisi, R., Swaters, R.A. & van Albada, T.S. 2005, A&A, 442, 137
- Osterbrock, D.E. 1989, *Astrophysics of Gaseous Nebulae and Active Galactic Nuclei* (Mill Valley: University Science Books)
- Peterson, B.M. 1997, *An Introduction to Active Galactic Nuclei* (Cambridge: Cambridge University Press)
- Peterson, B.M., Ferrarese, L., Gilbert, K.M., Kaspi, S., Malkan, M.A., Maoz, D., Merritt, D., Netzer, H., Onken, C.A., Pogge, R.W., Vestergaard, M. & Wandel, A. 2004, ApJ, 613, 682
- Rieke, G.H. 1978, ApJ, 226, 550
- Ruiz, J.R., Crenshaw, D.M., Kraemer, S.B., Bower, G.A., Gull, T.R., Hutchings, J.B., Kaiser, M.E. & Weistrop, D. 2001, AJ, 122, 2961
- Sako, M., Kahn, S.M., Paerels, F. & Liedahl, A. 2000, ApJ, 543, 115
- Savage, B.D. & Mathis, J.S. 1979, ARA&A, 17, 73
- Schlegel, D.J., Finkbeiner, D.P. & Davis, M. 1998, ApJ, 500, 525

- Schmidt, G.D. & Miller, J.S. 1985, ApJ, 290, 517
- Schmitt, H.R., & Kinney, A.L. 1996, ApJ, 463, 498
- Schmitt, H.R., & Kinney, A.L. 2000, ApJS, 128, 479
- Schmitt, H.R., Donley, J.L., Antonucci, R.R.J., Hutchings, J.B., & Kinney, A.L. 2003, ApJS, 148, 327
- Seab, C.G. & Shull, J.M. 1983, ApJ, 275, 652
- Seaton, M.J. 1978, MNRAS, 185, 5P
- Snow, T.P. & Witt, A.N. 1996, ApJ, 65L
- Staveley-Smith, L., Kim, S., Calbretta, M.R., Haynes, R.F. & Kesteven, M.J. 2003, MNRAS, 339, 87
- Swaters, R.A., van Albada, T.S., van der Hulst, J.M. & Sancisi, R. 2002, A&A, 390, 829
- Tifft, W.G. & Cocke, W.J. 1988, ApJS, 67, 1
- Turner, J., George, I.M., Nandra, K. & Mushotzky, R.F. 1997, ApJ, 488, 164
- Ulvestad, J.S., Roy, A.L., Colbert, E.J.M., Wilson, A.S, 1998, ApJ, 496, 196
- Weedman, D.W, Hao, L., Higdon, S.J.U., Devost, D., Yanling, W., Charmandaris, V., Brandl, B., Bass, E. & Houck, J.R. 2005, ApJ, 633, 706
- Welch, G.A., Sage, L.J. & Mitchell, G.F. 1998, ApJ, 499, 209
- Woo, J.-H., & Urry, C.M. 2002, ApJ, 579, 530

Fig. 1.— The structure of [O II] $\lambda 3727$ (thick grey lines) emission compared to [O III] $\lambda 4959$ (thin black lines). The thin black lines near velocity $+2000 \text{ km s}^{-1}$ are contours from the neighboring [O III] $\lambda 5007$ line. The contours are the 15%, 25%, 40%, 60%, 80%, and 95% flux levels relative to the peak value for the line of interest. The velocity resolution is two detector elements or 316 km s^{-1} . The spatial resolution is $0''.1$. The heavy black tick marks on the y-axis indicate the limits of the measurement bins.

Fig. 2.— The structure of [Ne V] $\lambda 3426$ (thick grey lines) emission compared to [O III] $\lambda 4959$ (thin black lines). The details of the plot are as described in the caption for Figure 1.

Fig. 3.— The effects of various absorbers on the model intrinsic continuum (grey line in all panels) are shown. Top left: filtered continuum (black line) illuminating gas within nominal bi-cone; absorber properties are $N_H = 10^{20.4} \text{ cm}^{-2}$ and $\log_{10} U = -1.5$. Top right: filtered continuum (absorber properties: $N_H = 10^{20.7} \text{ cm}^{-2}$ and $\log_{10} U = -2.5$) illuminating gas outside the nominal bi-cone envelope. Bottom left: filtered continuum (absorber properties: $N_H = 10^{21.6} \text{ cm}^{-2}$ and $\log_{10} U = -1.5$) illuminating gas outside the nominal bi-cone envelope. Bottom right: filtered continuum (absorber properties: $N_H = 10^{21.9} \text{ cm}^{-2}$ and $\log_{10} U = -3.0$) illuminating gas outside the nominal bi-cone envelope.

Fig. 4.— In this schematic diagram the arrow indicates the observer's line of sight. The vertical black line is the sky plane. The darker grey bi-cone cross section indicates the nominal hollow bi-cone of Ruiz et al. (2001). The diamonds in this region indicate the distances from the AGN used in the CLOUDY models for the co-located high and medium state ionization components that correspond to the measured kinematic components. The lighter grey region indicates the location of the low ionization state gas outside the bi-cone. The crosses indicate the distances from the AGN used in the CLOUDY models for the low ionization state components. Redshifted kinematic components are to the right of the sky plane, and blueshifted components are to the left. The thick grey line shows the orientation of the host galaxy plane (see Paper I and references therein).

Fig. 5.— Logarithm of the hydrogen volume number density for high ionization state model clouds as a function of radial distance from the AGN. Redshifted components are shown as open squares while blueshifted components are represented by solid squares. The horizontal bars represent the deprojected heights of the measurement bins. The solid curves represent functional forms for the hydrogen density vs. radial distance from the AGN. The curve labels indicate the power of $(1/r)$ for the density dependence.

Fig. 6.— Logarithm of the hydrogen volume number density for medium ionization state model clouds as a function of radial distance from the AGN. See the Figure 5 caption for a description of the plot symbols.

Fig. 7.— Logarithm of the hydrogen volume number density for low ionization state model clouds as a function of radial distance from the AGN. See the Figure 5 caption for a description of the plot symbols.

Table 1. CLOUDY Photoionization Model Input Parameters

Bin	Model Component	Distance (pc)	Screen U	Screen N_c (cm^{-2})	Fractional Contribution	n_H (cm^{-3})	N_c (cm^{-2})
(1)	(2)	(3)	(4)	(5)	(6)	(7)	(8)
(0''5E, r, 0''3)	high	143	$10^{-1.5}$	$10^{20.4}$	0.35	$10^{2.74}$	$10^{22.5}$
	med.	143	$10^{-1.5}$	$10^{20.4}$	0.35	$10^{4.68}$	$10^{20.0}$
	low	155	$10^{-2.5}$	$10^{20.7}$	0.30	$10^{2.84}$	$10^{22.5}$
(0''3E, b, 0''3)	high	73	$10^{-1.5}$	$10^{20.4}$	0.25	$10^{3.49}$	$10^{22.0}$
	med.	73	$10^{-1.5}$	$10^{20.4}$	0.45	$10^{4.99}$	$10^{21.1}$
	low	82	$10^{-3.0}$	$10^{21.9}$	0.30	$10^{3.16}$	$10^{22.0}$
(0''3E, r, 0''3)	high	68	$10^{-1.5}$	$10^{20.4}$	0.25	$10^{3.99}$	$10^{21.5}$
	med.	68	$10^{-1.5}$	$10^{20.4}$	0.45	$10^{5.49}$	$10^{20.7}$
	low	74	$10^{-3.0}$	$10^{21.9}$	0.30	$10^{3.00}$	$10^{22.0}$
(0''0E, b, 0''3)	high	18	$10^{-1.5}$	$10^{20.4}$	0.70	$10^{5.00}$	$10^{22.0}$
	med.	18	$10^{-1.5}$	$10^{20.4}$	0.00
	low	21	$10^{-1.5}$	$10^{21.6}$	0.30	$10^{4.00}$	$10^{23.0}$
(0''0W, r, 0''3)	high	18	$10^{-1.5}$	$10^{20.4}$	0.20	$10^{4.85}$	$10^{21.5}$
	med.	18	$10^{-1.5}$	$10^{20.4}$	0.50	$10^{5.00}$	$10^{22.3}$
	low	21	$10^{-1.5}$	$10^{21.6}$	0.30	$10^{4.25}$	$10^{23.5}$
(-0''3W, b, 0''3)	high	68	$10^{-1.5}$	$10^{20.4}$	0.40	$10^{3.84}$	$10^{22.0}$
	med.	68	$10^{-1.5}$	$10^{20.4}$	0.30	$10^{4.84}$	$10^{20.0}$
	low	74	$10^{-1.5}$	$10^{21.6}$	0.30	$10^{3.32}$	$10^{22.5}$
(-0''3W, r, 0''3)	high	73	$10^{-1.5}$	$10^{20.4}$	0.40	$10^{3.50}$	$10^{22.5}$
	med.	73	$10^{-1.5}$	$10^{20.4}$	0.30	$10^{4.50}$	$10^{20.5}$
	low	82	$10^{-1.5}$	$10^{21.6}$	0.30	$10^{3.25}$	$10^{22.0}$
(-0''5W, b, 0''2)	high	130	$10^{-1.5}$	$10^{20.4}$	0.40	$10^{3.46}$	$10^{21.5}$
	med.	130	$10^{-1.5}$	$10^{20.4}$	0.30	$10^{4.46}$	$10^{20.5}$
	low	140	$10^{-1.5}$	$10^{21.6}$	0.30	$10^{2.85}$	$10^{22.0}$
(-0''5W, r, 0''2)	high	138	$10^{-1.5}$	$10^{20.4}$	0.40	$10^{2.86}$	$10^{22.0}$
	med.	138	$10^{-1.5}$	$10^{20.4}$	0.30	$10^{4.36}$	$10^{20.0}$
	low	156	$10^{-1.5}$	$10^{21.6}$	0.30	$10^{2.50}$	$10^{22.5}$
(-0''7W, r, 0''3)	high	211	$10^{-1.5}$	$10^{20.4}$	0.20	$10^{2.57}$	$10^{21.8}$
	med.	211	$10^{-1.5}$	$10^{20.4}$	0.45	$10^{3.57}$	$10^{21.0}$
	low	239	$10^{-1.5}$	$10^{21.6}$	0.35	$10^{2.25}$	$10^{22.0}$
(-1''0W, r, 0''3)	high	291	$10^{-1.5}$	$10^{20.4}$	0.10	$10^{2.08}$	$10^{21.0}$
	med.	291	$10^{-1.5}$	$10^{20.4}$	0.50	$10^{3.50}$	$10^{20.5}$
	low	329	$10^{-1.5}$	$10^{21.6}$	0.40	$10^{2.00}$	$10^{21.5}$

Table 2. Line Ratios (Relative to $H\beta$) from Model Components, Composite and Observations for Position ($0^{\prime}5E$, r, $0^{\prime}3$)

(1)	(2)	Line Match ^a	High-U Model ^b	Med.-U Model ^c	Low-U Model ^d	Composite Model	Observed Data ^e	Model/Data Ratio
(1)	(2)	(3)	(4)	(5)	(6)	(7)	(8)	(9)
$Ly\alpha$	1216	0	24.05	23.78	5.92	18.52	38.97 ± 38.35	0.5 ± 0.5
NV	1240	1	0.71	0.06	0.11	0.30	0.56 ± 0.84	0.5 ± 0.8
CIV	1549	1	4.02	0.88	0.74	1.93	1.82 ± 1.08	1.1 ± 0.7
CIII]	1909	0	0.12	1.88	1.59	1.18	3.43 ± 2.54	0.3 ± 0.2
CII]	2326	0	0.00	0.10	1.90	0.60	1.84 ± 1.17	0.3 ± 0.2
[NeIV]	2424	1	0.15	0.15	0.02	0.11	0.16 ± 0.14	0.7 ± 0.6
MgII	2798	1	0.01	0.24	2.45	0.82	1.03 ± 0.42	0.8 ± 0.3
[NeV]	3426	1	0.49	0.03	0.01	0.19	0.36 ± 0.17	0.5 ± 0.2
[OII]	3727	1	0.03	0.06	14.19	4.29	3.05 ± 1.34	1.4 ± 0.6
[NeIII]	3869	1	0.88	1.74	1.24	1.29	1.30 ± 0.56	1.0 ± 0.4
[SII]	4074	0	0.00	0.03	0.24	0.08	0.48 ± 0.20	0.2 ± 0.1
[OIII]	4363	1	0.12	0.23	0.04	0.13	0.21 ± 0.08	0.6 ± 0.2
HeII	4686	1	0.10	0.26	0.03	0.14	0.27 ± 0.11	0.5 ± 0.2
[OIII]	5007	1	14.59	18.40	1.95	12.13	9.75 ± 3.50	1.2 ± 0.4
[FeVII]	6087	1	0.04	0.01	0.01	0.02	0.03 ± 0.01	0.6 ± 0.2
[OI]	6300	1	0.00	0.00	1.67	0.50	0.92 ± 0.29	0.5 ± 0.2
$H\alpha$	6563	1	2.90	2.80	3.01	2.90	2.56 ± 0.82	1.1 ± 0.4
[NII]	6584	1	0.00	0.10	7.73	2.35	3.75 ± 1.18	0.6 ± 0.2
[SII]	6724	1	0.00	0.01	3.61	1.09	1.67 ± 0.38	0.7 ± 0.2
[SIII]	9532	1	0.01	1.09	1.78	0.92	1.21 ± 0.34	0.8 ± 0.2
$f_{H\beta}^{model}$ ^f	4861	...	0.35	-0.22	-0.44	0.04
$f_{H\beta}^{data}$ ^g	4861	38.12 ± 9.85	...

^a1=Model and data line ratios relative to $H\beta$ match within a factor of 2; 0=no match.

^bHigh-U model. Boundary: m; $\log_{10}(U) = -0.29$; $\log_{10}(n_H) = 2.74 \text{ cm}^{-3}$; cloud $\log_{10}(N_c) = 22.5 \text{ cm}^{-2}$; fractional contribution = 0.35.

^cMedium-U model. Boundary: m; $\log_{10}(U) = -2.23$; $\log_{10}(n_H) = 4.68 \text{ cm}^{-3}$; cloud $\log_{10}(N_c) = 20.0 \text{ cm}^{-2}$; fractional contribution = 0.35.

^dLow-U model. Boundary: m; $\log_{10}(U) = -2.69$; $\log_{10}(n_H) = 2.84 \text{ cm}^{-3}$; cloud $\log_{10}(N_c) = 22.5 \text{ cm}^{-2}$; fractional contribution = 0.30; screen $\log_{10}(N_c) = 20.7 \text{ cm}^{-2}$.

^eWe corrected all observed fluxes for Galactic extinction using the Savage & Mathis (1979) extinction curve with $E(B-V) = 0.19$. We applied an additional correction for Mrk 3 internal extinction using the LMC curve of Koornneef & Code (1981). For this measurement bin the internal extinction correction corresponded to $E(B-V) = 0.31$. See Paper I for details.

^fLogarithm of model $H\beta$ flux. Units: $\log_{10}(\text{ergs s}^{-1} \text{ cm}^{-2})$.

^gObserved $H\beta$ flux. Units: $10^{-15} \text{ ergs s}^{-1} \text{ cm}^{-2}$.

Table 3. Line Ratios (Relative to $H\beta$) from Model Components, Composite and Observations for Position ($0^{\circ}3E$, b, $0^{\circ}3$)

(1)	(2)	Line Match ^a	High-U Model ^b	Med.-U Model ^c	Low-U Model ^d	Composite Model	Observed Data ^e	Model/Data Ratio
(1)	(2)	(3)	(4)	(5)	(6)	(7)	(8)	(9)
$Ly\alpha$	1216	1	26.07	4.13	2.65	9.17	9.90 ± 7.97	0.9 ± 0.7
NV	1240	1	1.69	0.02	0.00	0.43	0.46 ± 0.76	0.9 ± 1.5
CIV	1549	0	11.44	0.61	0.55	3.30	0.57 ± 0.34	5.7 ± 3.4
CIII]	1909	1	0.32	1.64	0.03	0.83	1.65 ± 0.97	0.5 ± 0.3
CII]	2326	1	0.00	0.21	1.09	0.42	0.68 ± 0.36	0.6 ± 0.3
[NeIV]	2424	1	0.48	0.08	0.00	0.16	0.31 ± 0.15	0.5 ± 0.2
MgII	2798	1	0.02	0.61	2.88	1.14	0.73 ± 0.24	1.6 ± 0.5
[NeV]	3426	1	1.40	0.03	0.00	0.37	0.63 ± 0.24	0.6 ± 0.2
[OII]	3727	1	0.02	0.16	4.20	1.34	2.58 ± 0.93	0.5 ± 0.2
[NeIII]	3869	1	1.36	1.78	0.75	1.36	1.26 ± 0.44	1.1 ± 0.4
[SII]	4074	1	0.00	0.15	0.44	0.20	0.37 ± 0.13	0.5 ± 0.2
[OIII]	4363	1	0.29	0.23	0.00	0.18	0.15 ± 0.05	1.2 ± 0.4
HeII	4686	1	0.25	0.08	0.01	0.10	0.16 ± 0.05	0.6 ± 0.2
[OIII]	5007	1	20.57	15.98	0.02	12.34	11.34 ± 3.37	1.1 ± 0.3
[FeVII]	6087	1	0.10	0.01	0.00	0.03	0.03 ± 0.01	1.0 ± 0.3
[OI]	6300	1	0.00	0.33	3.06	1.07	1.15 ± 0.31	0.9 ± 0.2
$H\alpha$	6563	1	2.90	2.84	2.98	2.90	3.21 ± 0.86	0.9 ± 0.2
[NII]	6584	1	0.00	0.89	9.13	3.14	5.26 ± 1.38	0.6 ± 0.2
[SII]	6724	1	0.00	0.28	6.29	2.01	1.68 ± 0.31	1.2 ± 0.2
[SIII]	9532	1	0.01	1.11	1.55	0.96	1.03 ± 0.24	0.9 ± 0.2
$f_{H\beta}^{model}$ ^f	4861	...	0.52	1.01	-0.64	0.74
$f_{H\beta}^{data}$ ^g	4861	16.77 ± 3.59	...

^a1=Model and data line ratios relative to $H\beta$ match within a factor of 2; 0=no match.

^bHigh-U model. Boundary: m; $\log_{10}(U) = -0.45$; $\log_{10}(n_H) = 3.49 \text{ cm}^{-3}$; cloud $\log_{10}(N_c) = 22.0 \text{ cm}^{-2}$; fractional contribution = 0.25.

^cMedium-U model. Boundary: r; $\log_{10}(U) = -1.95$; $\log_{10}(n_H) = 4.99 \text{ cm}^{-3}$; cloud $\log_{10}(N_c) = 21.1 \text{ cm}^{-2}$; fractional contribution = 0.45.

^dLow-U model. Boundary: m; $\log_{10}(U) = -3.08$; $\log_{10}(n_H) = 3.16 \text{ cm}^{-3}$; cloud $\log_{10}(N_c) = 22.0 \text{ cm}^{-2}$; fractional contribution = 0.30; screen $\log_{10}(N_c) = 21.9 \text{ cm}^{-2}$.

^eWe corrected all observed fluxes for Galactic extinction using the Savage & Mathis (1979) extinction curve with $E(B-V) = 0.19$. We applied an additional correction for Mrk 3 internal extinction using the LMC curve of Koornneef & Code (1981). For this measurement bin the internal extinction correction corresponded to $E(B-V) = 0.26$. See Paper I for details.

^f Logarithm of model $H\beta$ flux. Units: $\log_{10}(\text{ergs s}^{-1} \text{ cm}^{-2})$.

^gObserved $H\beta$ flux. Units: $10^{-15} \text{ ergs s}^{-1} \text{ cm}^{-2}$.

Table 4. Line Ratios (Relative to $H\beta$) from Model Components, Composite and Observations for Position ($0^{\circ}3E$, r, $0^{\circ}3$)

(1)	(2)	Line Match ^a	High-U Model ^b	Med.-U Model ^c	Low-U Model ^d	Composite Model	Observed Data ^e	Model/Data Ratio
(1)	(2)	(3)	(4)	(5)	(6)	(7)	(8)	(9)
$Ly\alpha$	1216	1	28.43	8.17	2.76	11.61	19.97 ± 11.55	0.6 ± 0.3
NV	1240	1	0.89	0.01	0.01	0.23	0.22 ± 0.13	1.0 ± 0.6
CIV	1549	1	11.27	0.21	0.60	3.09	2.11 ± 0.74	1.5 ± 0.5
CIII]	1909	1	0.88	1.44	0.09	0.89	0.77 ± 0.32	1.2 ± 0.5
CII]	2326	1	0.00	0.37	1.77	0.69	0.81 ± 0.31	0.9 ± 0.3
[NeIV]	2424	0	0.63	0.01	0.00	0.16	0.38 ± 0.13	0.4 ± 0.1
MgII	2798	1	0.04	1.03	3.29	1.46	0.96 ± 0.23	1.5 ± 0.4
[NeV]	3426	1	1.24	0.00	0.00	0.31	0.41 ± 0.12	0.8 ± 0.2
[OII]	3727	1	0.02	0.10	7.63	2.34	3.03 ± 0.80	0.8 ± 0.2
[NeIII]	3869	1	1.54	1.62	1.01	1.42	1.29 ± 0.33	1.1 ± 0.3
[SII]	4074	1	0.00	0.25	0.47	0.25	0.48 ± 0.12	0.5 ± 0.1
[OIII]	4363	1	0.34	0.24	0.00	0.19	0.17 ± 0.04	1.1 ± 0.3
HeII	4686	1	0.27	0.06	0.01	0.10	0.17 ± 0.04	0.6 ± 0.1
[OIII]	5007	1	23.64	10.60	0.06	10.70	11.17 ± 2.44	1.0 ± 0.2
[FeVII]	6087	1	0.16	0.00	0.00	0.04	0.04 ± 0.01	1.1 ± 0.3
[OI]	6300	1	0.00	0.38	2.88	1.04	1.28 ± 0.25	0.8 ± 0.2
$H\alpha$	6563	1	2.89	2.82	2.94	2.87	3.28 ± 0.70	0.9 ± 0.2
[NII]	6584	1	0.00	0.81	9.17	3.12	5.09 ± 1.01	0.6 ± 0.1
[SII]	6724	1	0.00	0.17	5.59	1.76	2.43 ± 0.33	0.7 ± 0.1
[SIII]	9532	0	0.03	1.16	1.66	1.03	2.13 ± 0.37	0.5 ± 0.1
$f_{H\beta}^{model}$ ^f	4861	...	0.53	1.15	-0.54	0.86
$f_{H\beta}^{data}$ ^g	4861	28.97 ± 4.71	...

^a1=Model and data line ratios relative to $H\beta$ match within a factor of 2; 0=no match.

^bHigh-U model. Boundary: m; $\log_{10}(U) = -0.89$; $\log_{10}(n_H) = 3.99 \text{ cm}^{-3}$; cloud $\log_{10}(N_c) = 21.5 \text{ cm}^{-2}$; fractional contribution = 0.25.

^cMedium-U model. Boundary: r; $\log_{10}(U) = -2.39$; $\log_{10}(n_H) = 5.49 \text{ cm}^{-3}$; cloud $\log_{10}(N_c) = 20.7 \text{ cm}^{-2}$; fractional contribution = 0.45.

^dLow-U model. Boundary: m; $\log_{10}(U) = -2.83$; $\log_{10}(n_H) = 3.00 \text{ cm}^{-3}$; cloud $\log_{10}(N_c) = 22.0 \text{ cm}^{-2}$; fractional contribution = 0.30; screen $\log_{10}(N_c) = 21.9 \text{ cm}^{-2}$.

^eWe corrected all observed fluxes for Galactic extinction using the Savage & Mathis (1979) extinction curve with $E(B-V) = 0.19$. We applied an additional correction for Mrk 3 internal extinction using the LMC curve of Koornneef & Code (1981). For this measurement bin the internal extinction correction corresponded to $E(B-V) = 0.24$. See Paper I for details.

^fLogarithm of model $H\beta$ flux. Units: $\log_{10}(\text{ergs s}^{-1} \text{ cm}^{-2})$.

^gObserved $H\beta$ flux. Units: $10^{-15} \text{ ergs s}^{-1} \text{ cm}^{-2}$.

Table 5. Line Ratios (Relative to $H\beta$) from Model Components, Composite and Observations for Position (0'0E, b, 0'3)

(1)	(2)	Line Match ^a	High-U Model ^b	Med.-U Model ^c	Low-U Model ^d	Composite Model	Observed Data ^e	Model/Data Ratio
(1)	(2)	(3)	(4)	(5)	(6)	(7)	(8)	(9)
Ly α	1216	0	36.59	...	4.39	26.93	6.78 \pm 4.69	4.0 \pm 2.8
NV	1240	1	0.67	...	0.14	0.51	0.40 \pm 0.28	1.3 \pm 0.9
CIV	1549	0	7.30	...	1.79	5.65	0.41 \pm 0.22	13.7 \pm 7.4
CIII]	1909	1	0.50	...	0.79	0.59	0.71 \pm 0.39	0.8 \pm 0.4
CII]	2326	1	0.00	...	2.85	0.85	0.60 \pm 0.27	1.4 \pm 0.6
[NeIV]	2424	1	0.21	...	0.02	0.15	0.22 \pm 0.09	0.7 \pm 0.3
MgII	2798	0	0.03	...	3.81	1.16	0.40 \pm 0.11	2.9 \pm 0.8
[NeV]	3426	1	0.69	...	0.02	0.49	0.44 \pm 0.16	1.1 \pm 0.4
[OII]	3727	1	0.00	...	7.59	2.28	2.44 \pm 0.78	0.9 \pm 0.3
[NeIII]	3869	1	1.50	...	1.20	1.41	0.99 \pm 0.33	1.4 \pm 0.5
[SII]	4074	1	0.00	...	0.86	0.26	0.17 \pm 0.07	1.5 \pm 0.6
[OIII]	4363	1	0.31	...	0.02	0.23	0.20 \pm 0.06	1.2 \pm 0.4
HeII	4686	1	0.12	...	0.01	0.09	0.13 \pm 0.04	0.6 \pm 0.2
[OIII]	5007	1	19.95	...	1.18	14.32	11.06 \pm 3.07	1.3 \pm 0.4
[FeVII]	6087	1	0.08	...	0.01	0.06	0.08 \pm 0.03	0.7 \pm 0.3
[OI]	6300	1	0.00	...	2.36	0.71	0.90 \pm 0.23	0.8 \pm 0.2
H α	6563	1	3.25	...	2.96	3.16	2.77 \pm 0.83	1.1 \pm 0.3
[NII]	6584	1	0.00	...	9.60	2.88	3.76 \pm 0.98	0.8 \pm 0.2
[SII]	6724	1	0.00	...	3.86	1.16	1.42 \pm 0.32	0.8 \pm 0.2
[SIII]	9532	1	0.05	...	1.84	0.59	1.09 \pm 0.28	0.5 \pm 0.1
$f_{H\beta}^{model}$ ^f	4861	...	2.05	...	1.25	1.92
$f_{H\beta}^{data}$ ^g	4861	18.87 \pm 3.67	...

^a1=Model and data line ratios relative to $H\beta$ match within a factor of 2; 0=no match.

^bHigh-U model. Boundary: m ; $\log_{10}(U) = -0.75$; $\log_{10}(n_H) = 5.00 \text{ cm}^{-3}$; cloud $\log_{10}(N_c) = 22.0 \text{ cm}^{-2}$; fractional contribution = 0.70.

^cNo medium-U model component required for this observed kinematic component.

^dLow-U model. Boundary: m ; $\log_{10}(U) = -2.52$; $\log_{10}(n_H) = 4.00 \text{ cm}^{-3}$; cloud $\log_{10}(N_c) = 23.0 \text{ cm}^{-2}$; fractional contribution = 0.30; screen $\log_{10}(N_c) = 21.6 \text{ cm}^{-2}$.

^eWe corrected all observed fluxes for Galactic extinction using the Savage & Mathis (1979) extinction curve with $E(B-V) = 0.19$. We applied an additional correction for Mrk 3 internal extinction using the LMC curve of Koornneef & Code (1981). For this measurement bin the internal extinction correction corresponded to $E(B-V) = 0.22$. See Paper I for details.

^fLogarithm of model $H\beta$ flux. Units: $\log_{10}(\text{ergs s}^{-1} \text{ cm}^{-2})$.

^gObserved $H\beta$ flux. Units: $10^{-15} \text{ ergs s}^{-1} \text{ cm}^{-2}$.

Table 6. Line Ratios (Relative to $H\beta$) from Model Components, Composite and Observations for Position ($0^{\circ}0'W$, r , $0^{\circ}3$)

(1)	(2)	Line Match ^a	High-U Model ^b	Med.-U Model ^c	Low-U Model ^d	Composite Model	Observed Data ^e	Model/Data Ratio
(1)	(2)	(3)	(4)	(5)	(6)	(7)	(8)	(9)
$Ly\alpha$	1216	0	34.80	1.37	2.19	8.30	54.35 ± 14.72	0.2 ± 0.1
NV	1240	1	5.10	1.05	0.06	1.56	2.46 ± 0.66	0.6 ± 0.2
CIV	1549	1	37.32	5.63	0.91	10.55	6.51 ± 1.12	1.6 ± 0.3
CIII]	1909	0	1.12	2.68	0.17	1.62	4.99 ± 1.07	0.3 ± 0.1
CII]	2326	1	0.00	0.46	1.23	0.60	1.13 ± 0.26	0.5 ± 0.1
[NeIV]	2424	1	1.26	0.72	0.00	0.61	1.17 ± 0.22	0.5 ± 0.1
MgII	2798	1	0.05	0.43	2.28	0.91	0.70 ± 0.12	1.3 ± 0.2
[NeV]	3426	1	4.31	1.93	0.00	1.83	1.43 ± 0.24	1.3 ± 0.2
[OII]	3727	1	0.00	0.32	2.75	0.98	1.39 ± 0.40	0.7 ± 0.2
[NeIII]	3869	1	1.71	3.42	0.57	2.22	1.72 ± 0.30	1.3 ± 0.2
[SII]	4074	1	0.00	0.52	0.68	0.46	0.36 ± 0.06	1.3 ± 0.2
[OIII]	4363	1	0.77	0.88	0.00	0.60	0.32 ± 0.05	1.9 ± 0.3
HeII	4686	1	0.67	0.23	0.01	0.25	0.32 ± 0.05	0.8 ± 0.1
[OIII]	5007	1	22.54	26.58	0.12	17.83	15.87 ± 2.61	1.1 ± 0.2
[FeVII]	6087	1	0.21	0.09	0.00	0.09	0.10 ± 0.02	0.9 ± 0.2
[OI]	6300	1	0.00	2.02	2.14	1.65	0.88 ± 0.16	1.9 ± 0.3
$H\alpha$	6563	1	2.79	2.87	3.08	2.92	3.31 ± 0.69	0.9 ± 0.2
[NII]	6584	1	0.00	1.34	7.45	2.90	3.16 ± 0.49	0.9 ± 0.1
[SII]	6724	1	0.00	2.18	3.82	2.24	2.45 ± 0.44	0.9 ± 0.2
[SIII]	9532	1	0.00	1.01	1.28	0.89	1.48 ± 0.22	0.6 ± 0.1
$f_{H\beta}^{model}$ ^f	4861	...	1.25	1.66	1.47	1.55
$f_{H\beta}^{data}$ ^g	4861	33.79 ± 4.56	...

^a1=Model and data line ratios relative to $H\beta$ match within a factor of 2; 0=no match.

^bHigh-U model. Boundary: m ; $\log_{10}(U) = -0.60$; $\log_{10}(n_H) = 4.85 \text{ cm}^{-3}$; cloud $\log_{10}(N_c) = 21.5 \text{ cm}^{-2}$; fractional contribution = 0.20.

^cMedium-U model. Boundary: r ; $\log_{10}(U) = -0.75$; $\log_{10}(n_H) = 5.00 \text{ cm}^{-3}$; cloud $\log_{10}(N_c) = 22.3 \text{ cm}^{-2}$; fractional contribution = 0.50.

^dLow-U model. Boundary: m ; $\log_{10}(U) = -2.77$; $\log_{10}(n_H) = 4.25 \text{ cm}^{-3}$; cloud $\log_{10}(N_c) = 23.5 \text{ cm}^{-2}$; fractional contribution = 0.30; screen $\log_{10}(N_c) = 21.6 \text{ cm}^{-2}$.

^eWe corrected all observed fluxes for Galactic extinction using the Savage & Mathis (1979) extinction curve with $E(B-V) = 0.19$. We applied an additional correction for Mrk 3 internal extinction using the LMC curve of Koornneef & Code (1981). For this measurement bin the internal extinction correction corresponded to $E(B-V) = 0.40$. See Paper I for details.

^fLogarithm of model $H\beta$ flux. Units: $\log_{10}(\text{ergs s}^{-1} \text{ cm}^{-2})$.

^gObserved $H\beta$ flux. Units: $10^{-15} \text{ ergs s}^{-1} \text{ cm}^{-2}$.

Table 7. Line Ratios (Relative to $H\beta$) from Model Components, Composite and Observations for Position ($-0'3W$, b , $0'3$)

(1)	(2)	Line Match ^a	High-U Model ^b	Med.-U Model ^c	Low-U Model ^d	Composite Model	Observed Data ^e	Model/Data Ratio
(1)	(2)	(3)	(4)	(5)	(6)	(7)	(8)	(9)
$Ly\alpha$	1216	1	28.14	27.01	6.60	21.34	18.58 ± 5.76	1.1 ± 0.3
NV	1240	1	0.49	0.53	0.03	0.36	0.69 ± 0.22	0.5 ± 0.2
CIV	1549	1	5.08	10.96	2.14	5.96	3.06 ± 0.60	1.9 ± 0.4
CIII]	1909	1	0.35	5.13	0.14	1.72	1.36 ± 0.37	1.3 ± 0.4
CII]	2326	1	0.00	0.06	1.15	0.36	0.64 ± 0.13	0.6 ± 0.1
[NeIV]	2424	1	0.25	1.53	0.00	0.56	0.46 ± 0.09	1.2 ± 0.2
MgII	2798	1	0.02	0.12	2.36	0.75	0.75 ± 0.10	1.0 ± 0.1
[NeV]	3426	1	0.57	0.99	0.00	0.52	0.78 ± 0.12	0.7 ± 0.1
[OII]	3727	1	0.02	0.02	5.35	1.62	2.60 ± 0.36	0.6 ± 0.1
[NeIII]	3869	1	1.11	2.19	0.74	1.32	1.38 ± 0.19	1.0 ± 0.1
[SII]	4074	1	0.00	0.00	0.42	0.13	0.17 ± 0.04	0.8 ± 0.2
[OIII]	4363	1	0.17	0.64	0.00	0.26	0.29 ± 0.04	0.9 ± 0.1
HeII	4686	1	0.11	0.74	0.01	0.27	0.21 ± 0.03	1.3 ± 0.2
[OIII]	5007	1	17.75	23.59	0.06	14.19	13.84 ± 1.63	1.0 ± 0.1
[FeVII]	6087	1	0.07	0.20	0.00	0.09	0.11 ± 0.02	0.8 ± 0.1
[OI]	6300	1	0.00	0.00	2.60	0.78	0.96 ± 0.10	0.8 ± 0.1
$H\alpha$	6563	1	3.07	2.74	2.97	2.94	3.67 ± 0.38	0.8 ± 0.1
[NII]	6584	1	0.00	0.02	8.51	2.56	5.07 ± 0.50	0.5 ± 0.0
[SII]	6724	1	0.00	0.00	5.26	1.58	2.15 ± 0.16	0.7 ± 0.1
[SIII]	9532	0	0.05	0.37	1.63	0.62	1.48 ± 0.13	0.4 ± 0.0
$f_{H\beta}^{model}$ ^f	4861	...	0.94	-0.15	-0.04	0.60
$f_{H\beta}^{data}$ ^g	4861	11.71 ± 0.96	...

^a1=Model and data line ratios relative to $H\beta$ match within a factor of 2; 0=no match.

^bHigh-U model. Boundary: m ; $\log_{10}(U) = -0.74$; $\log_{10}(n_H) = 3.84 \text{ cm}^{-3}$; cloud $\log_{10}(N_c) = 22.0 \text{ cm}^{-2}$; fractional contribution = 0.40.

^cMedium-U model. Boundary: m ; $\log_{10}(U) = -1.74$; $\log_{10}(n_H) = 4.84 \text{ cm}^{-3}$; cloud $\log_{10}(N_c) = 20.0 \text{ cm}^{-2}$; fractional contribution = 0.30.

^dLow-U model. Boundary: m ; $\log_{10}(U) = -2.95$; $\log_{10}(n_H) = 3.32 \text{ cm}^{-3}$; cloud $\log_{10}(N_c) = 22.5 \text{ cm}^{-2}$; fractional contribution = 0.30; screen $\log_{10}(N_c) = 21.6 \text{ cm}^{-2}$.

^eWe corrected all observed fluxes for Galactic extinction using the Savage & Mathis (1979) extinction curve with $E(B-V) = 0.19$. We applied an additional correction for Mrk 3 internal extinction using the LMC curve of Koornneef & Code (1981). For this measurement bin the internal extinction correction corresponded to $E(B-V) = 0.22$. See Paper I for details.

^f Logarithm of model $H\beta$ flux. Units: $\log_{10}(\text{ergs s}^{-1} \text{ cm}^{-2})$.

^gObserved $H\beta$ flux. Units: $10^{-15} \text{ ergs s}^{-1} \text{ cm}^{-2}$.

Table 8. Line Ratios (Relative to $H\beta$) from Model Components, Composite and Observations for Position ($-0'3W$, r , $0'3$)

(1)	(2)	Line Match ^a	High-U Model ^b	Med.-U Model ^c	Low-U Model ^d	Composite Model	Observed Data ^e	Model/Data Ratio
(1)	(2)	(3)	(4)	(5)	(6)	(7)	(8)	(9)
$Ly\alpha$	1216	1	27.23	16.97	10.88	19.25	29.68 ± 7.08	0.6 ± 0.1
NV	1240	0	0.46	0.86	0.04	0.45	1.29 ± 0.31	0.3 ± 0.1
CIV	1549	1	3.30	13.27	3.34	6.30	6.28 ± 0.90	1.0 ± 0.1
CIII]	1909	1	0.67	4.51	0.19	1.68	2.20 ± 0.52	0.8 ± 0.2
CII]	2326	1	0.00	0.03	1.49	0.46	0.59 ± 0.09	0.8 ± 0.1
[NeIV]	2424	1	0.13	2.08	0.00	0.68	0.76 ± 0.11	0.9 ± 0.1
MgII	2798	1	0.04	0.08	2.96	0.93	1.05 ± 0.10	0.9 ± 0.1
[NeV]	3426	1	0.39	1.82	0.00	0.70	1.07 ± 0.12	0.7 ± 0.1
[OII]	3727	1	0.03	0.02	7.08	2.14	2.45 ± 0.27	0.9 ± 0.1
[NeIII]	3869	1	1.17	2.29	0.93	1.43	1.38 ± 0.15	1.0 ± 0.1
[SII]	4074	1	0.00	0.00	0.45	0.13	0.27 ± 0.04	0.5 ± 0.1
[OIII]	4363	1	0.16	0.70	0.00	0.27	0.21 ± 0.03	1.3 ± 0.2
HeII	4686	1	0.07	0.64	0.01	0.22	0.23 ± 0.02	1.0 ± 0.1
[OIII]	5007	1	18.83	27.41	0.09	15.78	14.20 ± 1.35	1.1 ± 0.1
[FeVII]	6087	1	0.04	0.25	0.00	0.09	0.12 ± 0.01	0.8 ± 0.1
[OI]	6300	1	0.00	0.00	2.73	0.82	0.72 ± 0.06	1.1 ± 0.1
$H\alpha$	6563	1	3.17	2.75	2.93	2.97	2.48 ± 0.22	1.2 ± 0.1
[NII]	6584	1	0.00	0.01	8.93	2.68	3.25 ± 0.27	0.8 ± 0.1
[SII]	6724	1	0.00	0.00	4.85	1.45	1.58 ± 0.09	0.9 ± 0.1
[SIII]	9532	0	0.08	0.13	1.81	0.61	1.85 ± 0.13	0.3 ± 0.0
$f_{H\beta}^{model}$ ^f	4861	...	1.08	-0.02	-0.35	0.72
$f_{H\beta}^{data}$ ^g	4861	14.10 ± 0.94	...

^a1=Model and data line ratios relative to $H\beta$ match within a factor of 2; 0=no match.

^bHigh-U model. Boundary: m ; $\log_{10}(U) = -0.46$; $\log_{10}(n_H) = 3.50 \text{ cm}^{-3}$; cloud $\log_{10}(N_c) = 22.5 \text{ cm}^{-2}$; fractional contribution = 0.40.

^cMedium-U model. Boundary: m ; $\log_{10}(U) = -1.46$; $\log_{10}(n_H) = 4.50 \text{ cm}^{-3}$; cloud $\log_{10}(N_c) = 20.5 \text{ cm}^{-2}$; fractional contribution = 0.30.

^dLow-U model. Boundary: m ; $\log_{10}(U) = -2.98$; $\log_{10}(n_H) = 3.25 \text{ cm}^{-3}$; cloud $\log_{10}(N_c) = 22.0 \text{ cm}^{-2}$; fractional contribution = 0.30; screen $\log_{10}(N_c) = 21.6 \text{ cm}^{-2}$.

^eWe corrected all observed fluxes for Galactic extinction using the Savage & Mathis (1979) extinction curve with $E(B-V) = 0.19$. We applied an additional correction for Mrk 3 internal extinction using the LMC curve of Koornneef & Code (1981). For this measurement bin the internal extinction correction corresponded to $E(B-V) = 0.21$. See Paper I for details.

^f Logarithm of model $H\beta$ flux. Units: $\log_{10}(\text{ergs s}^{-1} \text{ cm}^{-2})$.

^gObserved $H\beta$ flux. Units: $10^{-15} \text{ ergs s}^{-1} \text{ cm}^{-2}$.

Table 9. Line Ratios (Relative to $H\beta$) from Model Components, Composite and Observations for Position ($-0''.5W$, b , $0''.2$)

(1)	(2)	Line Match ^a	High-U Model ^b	Med.-U Model ^c	Low-U Model ^d	Composite Model	Observed Data ^e	Model/Data Ratio
(1)	(2)	(3)	(4)	(5)	(6)	(7)	(8)	(9)
$Ly\alpha$	1216	1	25.48	13.99	11.42	17.81	14.08 ± 8.35	1.3 ± 0.8
NV	1240	1	0.62	0.06	0.03	0.27	0.49 ± 0.32	0.6 ± 0.4
CIV	1549	1	8.57	1.41	3.34	4.85	2.68 ± 0.96	1.8 ± 0.6
CIII]	1909	0	0.76	1.87	0.15	0.91	2.45 ± 1.03	0.4 ± 0.2
CII]	2326	1	0.00	0.05	1.21	0.38	0.69 ± 0.26	0.5 ± 0.2
[NeIV]	2424	1	0.54	0.26	0.00	0.29	0.50 ± 0.18	0.6 ± 0.2
MgII	2798	1	0.03	0.15	2.61	0.84	1.07 ± 0.27	0.8 ± 0.2
[NeV]	3426	1	0.99	0.09	0.00	0.42	0.66 ± 0.18	0.6 ± 0.2
[OII]	3727	1	0.03	0.05	6.19	1.89	2.08 ± 0.55	0.9 ± 0.2
[NeIII]	3869	1	1.36	1.78	0.82	1.33	1.17 ± 0.30	1.1 ± 0.3
[SII]	4074	1	0.00	0.01	0.35	0.11	0.10 ± 0.03	1.1 ± 0.3
[OIII]	4363	1	0.27	0.24	0.00	0.18	0.26 ± 0.07	0.7 ± 0.2
HeII	4686	1	0.24	0.20	0.01	0.16	0.15 ± 0.04	1.1 ± 0.3
[OIII]	5007	1	21.48	19.58	0.06	14.48	13.45 ± 2.90	1.1 ± 0.2
[FeVII]	6087	1	0.15	0.03	0.00	0.07	0.12 ± 0.16	0.6 ± 0.8
[OI]	6300	1	0.00	0.00	2.72	0.82	0.63 ± 0.12	1.3 ± 0.2
$H\alpha$	6563	1	2.86	2.81	2.95	2.87	2.63 ± 0.52	1.1 ± 0.2
[NII]	6584	1	0.00	0.05	8.66	2.61	4.75 ± 0.94	0.6 ± 0.1
[SII]	6724	1	0.00	0.01	5.23	1.57	0.93 ± 0.14	1.7 ± 0.3
[SIII]	9532	1	0.03	0.68	1.78	0.75	1.12 ± 0.19	0.7 ± 0.1
$f_{H\beta}^{model}$ ^f	4861	...	0.03	0.05	-0.83	-0.09
$f_{H\beta}^{data}$ ^g	4861	9.03 ± 1.41	...

^a1=Model and data line ratios relative to $H\beta$ match within a factor of 2; 0=no match.

^bHigh-U model. Boundary: m ; $\log_{10}(U) = -0.92$; $\log_{10}(n_H) = 3.46 \text{ cm}^{-3}$; cloud $\log_{10}(N_c) = 21.5 \text{ cm}^{-2}$; fractional contribution = 0.40.

^cMedium-U model. Boundary: m ; $\log_{10}(U) = -1.92$; $\log_{10}(n_H) = 4.46 \text{ cm}^{-3}$; cloud $\log_{10}(N_c) = 20.5 \text{ cm}^{-2}$; fractional contribution = 0.30.

^dLow-U model. Boundary: m ; $\log_{10}(U) = -3.04$; $\log_{10}(n_H) = 2.85 \text{ cm}^{-3}$; cloud $\log_{10}(N_c) = 22.0 \text{ cm}^{-2}$; fractional contribution = 0.30; screen $\log_{10}(N_c) = 21.6 \text{ cm}^{-2}$.

^eWe corrected all observed fluxes for Galactic extinction using the Savage & Mathis (1979) extinction curve with $E(B-V) = 0.19$. We applied an additional correction for Mrk 3 internal extinction using the LMC curve of Koornneef & Code (1981). For this measurement bin the internal extinction correction corresponded to $E(B-V) = 0.15$. See Paper I for details.

^f Logarithm of model $H\beta$ flux. Units: $\log_{10}(\text{ergs s}^{-1} \text{ cm}^{-2})$.

^gObserved $H\beta$ flux. Units: $10^{-15} \text{ ergs s}^{-1} \text{ cm}^{-2}$.

Table 10. Line Ratios (Relative to $H\beta$) from Model Components, Composite and Observations for Position ($-0'5W$, r , $0'2$)

(1)	(2)	Line Match ^a	High-U Model ^b	Med.-U Model ^c	Low-U Model ^d	Composite Model	Observed Data ^e	Model/Data Ratio
(1)	(2)	(3)	(4)	(5)	(6)	(7)	(8)	(9)
$Ly\alpha$	1216	1	24.30	24.06	7.18	19.09	21.30 ± 2.18	0.9 ± 0.1
NV	1240	1	2.12	0.25	0.08	0.95	1.05 ± 0.11	0.9 ± 0.1
CIV	1549	1	12.76	5.30	2.35	7.40	7.42 ± 0.52	1.0 ± 0.1
CIII]	1909	1	0.30	4.06	0.22	1.41	1.85 ± 0.13	0.8 ± 0.1
CII]	2326	1	0.00	0.07	1.41	0.44	0.57 ± 0.04	0.8 ± 0.1
[NeIV]	2424	1	0.54	0.99	0.00	0.51	0.91 ± 0.06	0.6 ± 0.0
MgII	2798	1	0.02	0.15	2.40	0.77	0.48 ± 0.04	1.6 ± 0.1
[NeV]	3426	1	1.64	0.39	0.00	0.77	1.04 ± 0.05	0.7 ± 0.0
[OII]	3727	1	0.02	0.06	8.24	2.50	1.64 ± 0.08	1.5 ± 0.1
[NeIII]	3869	1	1.30	2.29	0.87	1.47	1.47 ± 0.07	1.0 ± 0.0
[SII]	4074	1	0.00	0.01	0.33	0.10	0.19 ± 0.01	0.5 ± 0.0
[OIII]	4363	1	0.30	0.45	0.00	0.26	0.20 ± 0.02	1.3 ± 0.1
HeII	4686	1	0.31	0.59	0.01	0.30	0.29 ± 0.01	1.0 ± 0.0
[OIII]	5007	1	19.71	25.10	0.12	15.45	15.69 ± 0.59	1.0 ± 0.0
[FeVII]	6087	1	0.10	0.11	0.00	0.07	0.10 ± 0.01	0.7 ± 0.1
[OI]	6300	1	0.00	0.00	2.43	0.73	0.57 ± 0.02	1.3 ± 0.0
$H\alpha$	6563	1	2.80	2.78	2.97	2.84	2.30 ± 0.20	1.2 ± 0.1
[NII]	6584	1	0.00	0.05	8.53	2.57	2.44 ± 0.08	1.1 ± 0.0
[SII]	6724	1	0.00	0.01	5.34	1.60	1.16 ± 0.03	1.4 ± 0.0
[SIII]	9532	1	0.00	0.60	1.74	0.70	1.24 ± 0.04	0.6 ± 0.0
$f_{H\beta}^{model}$ ^f	4861	...	-0.13	-0.60	-0.71	-0.37
$f_{H\beta}^{data}$ ^g	4861	20.81 ± 0.57	...

^a1=Model and data line ratios relative to $H\beta$ match within a factor of 2; 0=no match.

^bHigh-U model. Boundary: m ; $\log_{10}(U) = -0.38$; $\log_{10}(n_H) = 2.86 \text{ cm}^{-3}$; cloud $\log_{10}(N_c) = 22.0 \text{ cm}^{-2}$; fractional contribution = 0.40.

^cMedium-U model. Boundary: m ; $\log_{10}(U) = -1.88$; $\log_{10}(n_H) = 4.36 \text{ cm}^{-3}$; cloud $\log_{10}(N_c) = 20.0 \text{ cm}^{-2}$; fractional contribution = 0.30.

^dLow-U model. Boundary: m ; $\log_{10}(U) = -2.78$; $\log_{10}(n_H) = 2.50 \text{ cm}^{-3}$; cloud $\log_{10}(N_c) = 22.5 \text{ cm}^{-2}$; fractional contribution = 0.30; screen $\log_{10}(N_c) = 21.6 \text{ cm}^{-2}$.

^eWe corrected all observed fluxes for Galactic extinction using the Savage & Mathis (1979) extinction curve with $E(B-V) = 0.19$. We applied an additional correction for Mrk 3 internal extinction using the LMC curve of Koornneef & Code (1981). For this measurement bin the internal extinction correction corresponded to $E(B-V) = 0.16$. See Paper I for details.

^f Logarithm of model $H\beta$ flux. Units: $\log_{10}(\text{ergs s}^{-1} \text{ cm}^{-2})$.

^gObserved $H\beta$ flux. Units: $10^{-15} \text{ ergs s}^{-1} \text{ cm}^{-2}$.

Table 11. Line Ratios (Relative to $H\beta$) from Model Components, Composite and Observations for Position ($-0''.7W$, r, $0''.3$)

(1)	(2)	Line Match ^a	High-U Model ^b	Med.-U Model ^c	Low-U Model ^d	Composite Model	Observed Data ^e	Model/Data Ratio
(1)	(2)	(3)	(4)	(5)	(6)	(7)	(8)	(9)
$Ly\alpha$	1216	1	24.38	5.26	11.76	11.36	20.81 ± 1.48	0.5 ± 0.0
NV	1240	1	3.27	0.16	0.07	0.75	0.98 ± 0.42	0.8 ± 0.3
CIV	1549	1	20.71	2.80	3.54	6.64	5.04 ± 0.30	1.3 ± 0.1
CIII]	1909	0	0.55	1.77	0.22	0.98	2.09 ± 0.14	0.5 ± 0.0
CII]	2326	1	0.00	0.02	1.46	0.52	0.62 ± 0.03	0.8 ± 0.0
[NeIV]	2424	1	0.94	0.57	0.00	0.45	0.78 ± 0.08	0.6 ± 0.1
MgII	2798	1	0.04	0.09	2.69	0.99	0.90 ± 0.04	1.1 ± 0.0
[NeV]	3426	1	2.80	0.43	0.00	0.75	0.76 ± 0.03	1.0 ± 0.0
[OII]	3727	1	0.02	0.08	8.46	3.00	1.72 ± 0.06	1.7 ± 0.1
[NeIII]	3869	1	1.46	1.99	0.94	1.52	1.43 ± 0.08	1.1 ± 0.1
[SII]	4074	1	0.00	0.00	0.32	0.11	0.20 ± 0.02	0.6 ± 0.1
[OIII]	4363	1	0.43	0.31	0.00	0.22	0.20 ± 0.02	1.1 ± 0.1
HeII	4686	1	0.51	0.21	0.01	0.20	0.24 ± 0.01	0.8 ± 0.0
[OIII]	5007	1	21.66	22.82	0.10	14.64	14.37 ± 0.56	1.0 ± 0.0
[FeVII]	6087	1	0.14	0.08	0.00	0.06	0.08 ± 0.01	0.8 ± 0.1
[OI]	6300	1	0.00	0.00	2.53	0.89	0.52 ± 0.02	1.7 ± 0.1
$H\alpha$	6563	1	2.74	2.83	2.93	2.85	3.12 ± 0.10	0.9 ± 0.0
[NII]	6584	1	0.00	0.02	8.51	2.99	2.59 ± 0.11	1.2 ± 0.1
[SII]	6724	1	0.00	0.00	4.97	1.74	0.95 ± 0.02	1.8 ± 0.0
[SIII]	9532	1	0.00	0.25	1.83	0.75	1.22 ± 0.04	0.6 ± 0.0
$f_{H\beta}^{model}$ ^f	4861	...	-0.73	-0.37	-1.29	-0.61
$f_{H\beta}^{data}$ ^g	4861	30.28 ± 0.69	...

^a1=Model and data line ratios relative to $H\beta$ match within a factor of 2; 0=no match.

^bHigh-U model. Boundary: m ; $\log_{10}(U) = -0.45$; $\log_{10}(n_H) = 2.57 \text{ cm}^{-3}$; cloud $\log_{10}(N_c) = 21.8 \text{ cm}^{-2}$; fractional contribution = 0.20.

^cMedium-U model. Boundary: m ; $\log_{10}(U) = -1.45$; $\log_{10}(n_H) = 3.57 \text{ cm}^{-3}$; cloud $\log_{10}(N_c) = 21.0 \text{ cm}^{-2}$; fractional contribution = 0.45.

^dLow-U model. Boundary: m ; $\log_{10}(U) = -2.90$; $\log_{10}(n_H) = 2.25 \text{ cm}^{-3}$; cloud $\log_{10}(N_c) = 22.0 \text{ cm}^{-2}$; fractional contribution = 0.35; screen $\log_{10}(N_c) = 21.6 \text{ cm}^{-2}$.

^eWe corrected all observed fluxes for Galactic extinction using the Savage & Mathis (1979) extinction curve with $E(B-V) = 0.19$. We applied an additional correction for Mrk 3 internal extinction using the LMC curve of Koornneef & Code (1981). For this measurement bin the internal extinction correction corresponded to $E(B-V) = 0.14$. See Paper I for details.

^f Logarithm of model $H\beta$ flux. Units: $\log_{10}(\text{ergs s}^{-1} \text{ cm}^{-2})$.

^gObserved $H\beta$ flux. Units: $10^{-15} \text{ ergs s}^{-1} \text{ cm}^{-2}$.

Table 12. Line Ratios (Relative to $H\beta$) from Model Components, Composite and Observations for Position ($-1''0W$, r , $0''3$)

(1)	(2)	Line Match ^a	High-U Model ^b	Med.-U Model ^c	Low-U Model ^d	Composite Model	Observed Data ^e	Model/Data Ratio
(1)	(2)	(3)	(4)	(5)	(6)	(7)	(8)	(9)
$Ly\alpha$	1216	0	32.25	12.53	24.86	19.43	42.54 ± 13.18	0.5 ± 0.2
NV	1240	1	7.59	0.18	0.08	0.88	0.86 ± 0.28	1.0 ± 0.3
CIV	1549	1	14.05	3.63	6.08	5.65	5.32 ± 1.00	1.1 ± 0.2
CIII]	1909	0	0.09	2.57	0.30	1.41	4.74 ± 6.71	0.3 ± 0.4
CII]	2326	0	0.00	0.03	1.53	0.63	1.66 ± 2.11	0.4 ± 0.5
[NeIV]	2424	1	0.17	0.77	0.00	0.40	0.76 ± 0.19	0.5 ± 0.1
MgII	2798	1	0.00	0.10	2.80	1.17	1.91 ± 0.24	0.6 ± 0.1
[NeV]	3426	1	2.89	0.41	0.00	0.49	0.53 ± 0.08	0.9 ± 0.1
[OII]	3727	1	0.00	0.11	8.98	3.65	4.05 ± 0.57	0.9 ± 0.1
[NeIII]	3869	1	0.00	2.07	0.96	1.42	1.36 ± 0.19	1.0 ± 0.1
[SII]	4074	1	0.00	0.00	0.26	0.10	0.07 ± 0.04	1.4 ± 0.8
[OIII]	4363	1	0.00	0.35	0.00	0.18	0.18 ± 0.04	1.0 ± 0.2
HeII	4686	1	0.90	0.38	0.01	0.29	0.25 ± 0.03	1.1 ± 0.1
[OIII]	5007	1	0.03	23.98	0.12	12.04	12.26 ± 1.41	1.0 ± 0.1
[FeVII]	6087	0	0.00	0.11	0.00	0.05
[OI]	6300	1	0.00	0.00	2.24	0.90	0.77 ± 0.08	1.2 ± 0.1
$H\alpha$	6563	1	2.60	2.81	2.90	2.82	3.52 ± 0.36	0.8 ± 0.1
[NII]	6584	1	0.00	0.03	7.54	3.03	4.27 ± 0.44	0.7 ± 0.1
[SII]	6724	1	0.00	0.01	3.65	1.46	2.03 ± 0.15	0.7 ± 0.1
[SIII]	9532	1	0.00	0.32	1.83	0.90	1.28 ± 0.12	0.7 ± 0.1
$f_{H\beta}^{model}$ ^f	4861	...	-2.05	-0.95	-1.83	-1.20
$f_{H\beta}^{data}$ ^g	4861	4.55 ± 0.38	...

^a1=Model and data line ratios relative to $H\beta$ match within a factor of 2; 0=no match.

^bHigh-U model. Boundary: m ; $\log_{10}(U) = -0.24$; $\log_{10}(n_H) = 2.08 \text{ cm}^{-3}$; cloud $\log_{10}(N_c) = 21.0 \text{ cm}^{-2}$; fractional contribution = 0.10.

^cMedium-U model. Boundary: m ; $\log_{10}(U) = -1.66$; $\log_{10}(n_H) = 3.50 \text{ cm}^{-3}$; cloud $\log_{10}(N_c) = 20.5 \text{ cm}^{-2}$; fractional contribution = 0.50.

^dLow-U model. Boundary: m ; $\log_{10}(U) = -2.93$; $\log_{10}(n_H) = 2.00 \text{ cm}^{-3}$; cloud $\log_{10}(N_c) = 21.5 \text{ cm}^{-2}$; fractional contribution = 0.40; screen $\log_{10}(N_c) = 21.6 \text{ cm}^{-2}$.

^eWe corrected all observed fluxes for Galactic extinction using the Savage & Mathis (1979) extinction curve with $E(B-V) = 0.19$. We applied an additional correction for Mrk 3 internal extinction using the LMC curve of Koornneef & Code (1981). For this measurement bin the internal extinction correction corresponded to $E(B-V) = 0.12$. See Paper I for details.

^fLogarithm of model $H\beta$ flux. Units: $\log_{10}(\text{ergs s}^{-1} \text{ cm}^{-2})$.

^gObserved $H\beta$ flux. Units: $10^{-15} \text{ ergs s}^{-1} \text{ cm}^{-2}$.

Table 13. CLOUDY Photoionization Model Output

Bin	Model	Bound ^a	U	H β Flux (erg s ⁻¹ cm ⁻²)	Emitting Area (pc ²)	Component Depth (pc)	Bin Depth (pc)	Component Height (pc)	Bin Height (pc)	Filling Factor	T _{avg.} (K)
(1)	(2)	(3)	(4)	(5)	(6)	(7)	(8)	(9)	(10)	(11)	(12)
(0'5E, r, 0'3)	high	m	10 ^{-0.29}	2.23 × 10 ⁺⁰⁰	211	8	26	19	79	10 ^{-1.12}	17000
	med.	m	10 ^{-2.23}	6.06 × 10 ⁻⁰¹	777	29	26	<1	79	10 ^{-5.00}	12000
	low	m	10 ^{-2.69}	3.63 × 10 ⁻⁰¹	1111	42	42	15	79	10 ^{-0.71}	9000
(0'3E, b, 0'3)	high	m	10 ^{-0.45}	3.33 × 10 ⁺⁰⁰	44	1	14	1	66	10 ^{-2.70}	16000
	med.	i	10 ^{-1.95}	1.04 × 10 ⁺⁰¹	25	0	14	<1	66	10 ^{-5.45}	10000
	low	m	10 ^{-3.09}	2.28 × 10 ⁻⁰¹	777	29	25	2	66	10 ^{-1.38}	8000
(0'3E, r, 0'3)	high	m	10 ^{-0.89}	3.43 × 10 ⁺⁰⁰	74	2	12	<1	66	10 ^{-3.42}	15000
	med.	i	10 ^{-2.39}	1.43 × 10 ⁺⁰¹	32	1	12	<1	66	10 ^{-6.09}	9000
	low	m	10 ^{-2.83}	2.91 × 10 ⁻⁰¹	1055	40	20	3	66	10 ^{-0.99}	9000
(0'0E, b, 0'3)	high	m	10 ^{-0.75}	1.10 × 10 ⁺⁰²	4	0	4	<1	66	10 ^{-4.64}	16000
	med.	m
	low	m	10 ^{-2.52}	1.80 × 10 ⁺⁰¹	11	0	6	3	66	10 ^{-2.46}	11000
(0'0W, r, 0'3)	high	m	10 ^{-0.60}	1.79 × 10 ⁺⁰¹	13	0	4	<1	66	10 ^{-4.49}	18000
	med.	i	10 ^{-0.75}	4.47 × 10 ⁺⁰¹	13	0	4	<1	66	10 ^{-3.84}	15000
	low	m	10 ^{-2.77}	2.93 × 10 ⁺⁰¹	12	0	6	6	66	10 ^{-2.17}	9000
(-0'3W, b, 0'3)	high	m	10 ^{-0.74}	8.75 × 10 ⁺⁰⁰	18	0	12	<1	66	10 ^{-3.37}	15000
	med.	m	10 ^{-1.74}	6.97 × 10 ⁻⁰¹	177	6	12	<1	66	10 ^{-5.40}	16000
	low	m	10 ^{-2.95}	9.30 × 10 ⁻⁰¹	133	5	20	5	66	10 ^{-1.71}	8000
(-0'3W, r, 0'3)	high	m	10 ^{-0.46}	1.19 × 10 ⁺⁰¹	16	0	14	3	66	10 ^{-2.64}	18000
	med.	m	10 ^{-1.46}	9.60 × 10 ⁻⁰¹	155	5	14	<1	66	10 ^{-4.67}	16000
	low	m	10 ^{-2.98}	4.48 × 10 ⁻⁰¹	333	12	25	2	66	10 ^{-1.84}	9000
(-0'5W, b, 0'2)	high	m	10 ^{-0.92}	1.04 × 10 ⁺⁰⁰	122	4	24	<1	53	10 ^{-2.86}	14000
	med.	m	10 ^{-1.92}	1.12 × 10 ⁺⁰⁰	85	3	24	<1	53	10 ^{-5.02}	13000
	low	m	10 ^{-3.04}	1.48 × 10 ⁻⁰¹	644	24	38	5	53	10 ^{-1.24}	8000
(-0'5W, r, 0'2)	high	m	10 ^{-0.38}	7.56 × 10 ⁻⁰¹	388	14	27	5	53	10 ^{-1.31}	17000
	med.	m	10 ^{-1.88}	2.48 × 10 ⁻⁰¹	888	34	27	<1	53	10 ^{-4.46}	14000
	low	m	10 ^{-2.78}	1.98 × 10 ⁻⁰¹	1111	42	47	33	53	10 ^{-0.25}	9000
(-0'7W, r, 0'3)	high	m	10 ^{-0.45}	1.92 × 10 ⁻⁰¹	1111	42	41	6	79	10 ^{-1.13}	17000
	med.	m	10 ^{-1.45}	4.33 × 10 ⁻⁰¹	1111	42	41	<1	79	10 ^{-2.93}	14000
	low	m	10 ^{-2.90}	5.10 × 10 ⁻⁰²	7333	282	72	19	79	10 ^{-0.04}	9000

Table 13—Continued

Bin	Model	Bound ^a	U	H β Flux (erg s ⁻¹ cm ⁻²)	Emitting Area (pc ²)	Component Depth (pc)	Bin Depth (pc)	Component Height (pc)	Bin Height (pc)	Filling Factor	T _{avg.} (K)
(1)	(2)	(3)	(4)	(5)	(6)	(7)	(8)	(9)	(10)	(11)	(12)
(-1''0W, r, 0''3)	high	m	10 ^{-0.24}	9.04 × 10 ⁻⁰³	1777	68	56	3	66	10 ^{-1.29}	26000
	med.	m	10 ^{-1.66}	1.13 × 10 ⁻⁰¹	711	27	56	<1	66	10 ^{-3.61}	13000
	low	m	10 ^{-2.93}	1.48 × 10 ⁻⁰²	4333	166	99	11	66	10 ^{-0.58}	10000

^a “m” indicates that the model cloud is matter bounded and “i” indicates that it is ionization bounded.

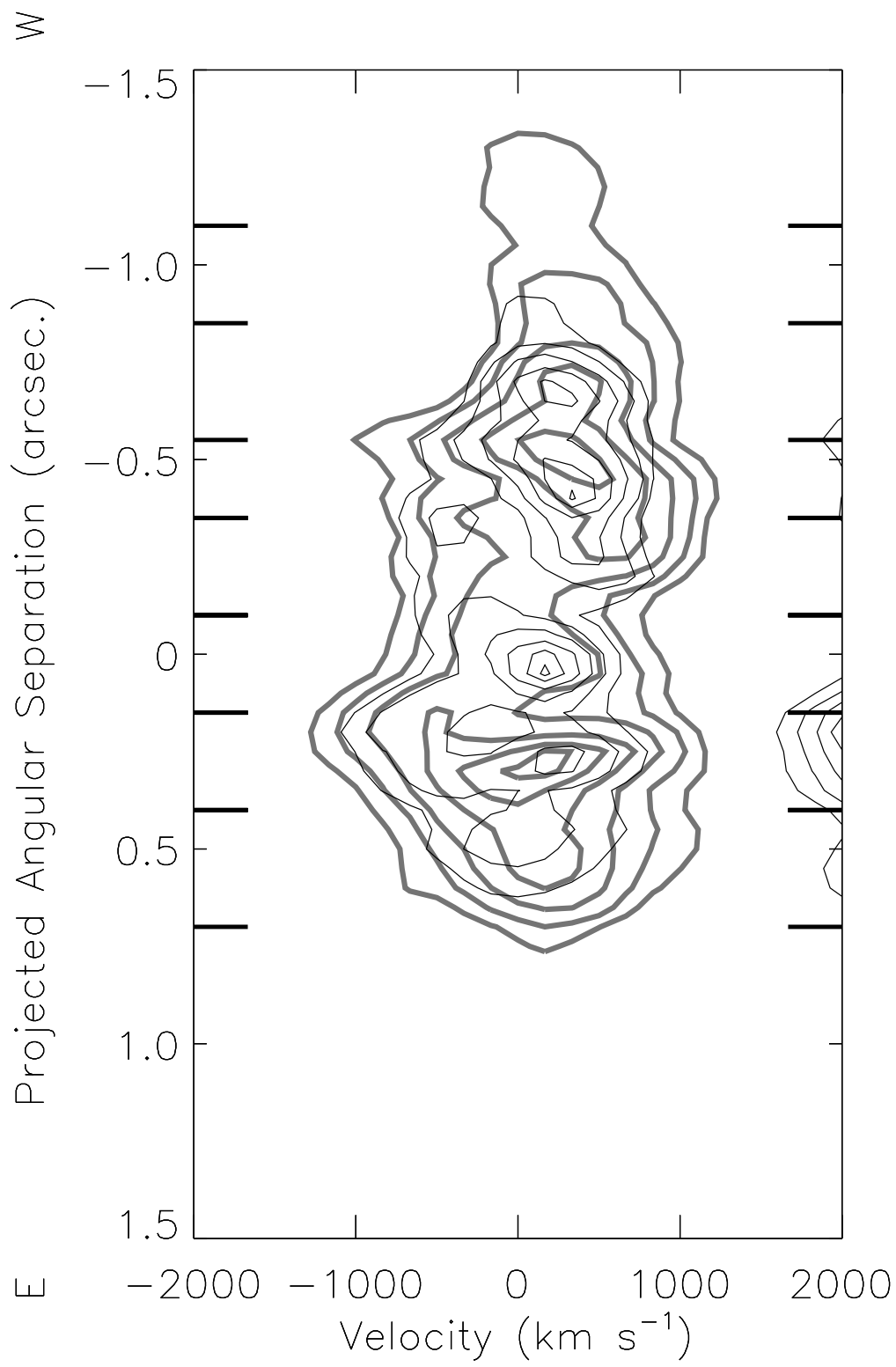


Fig. 1.

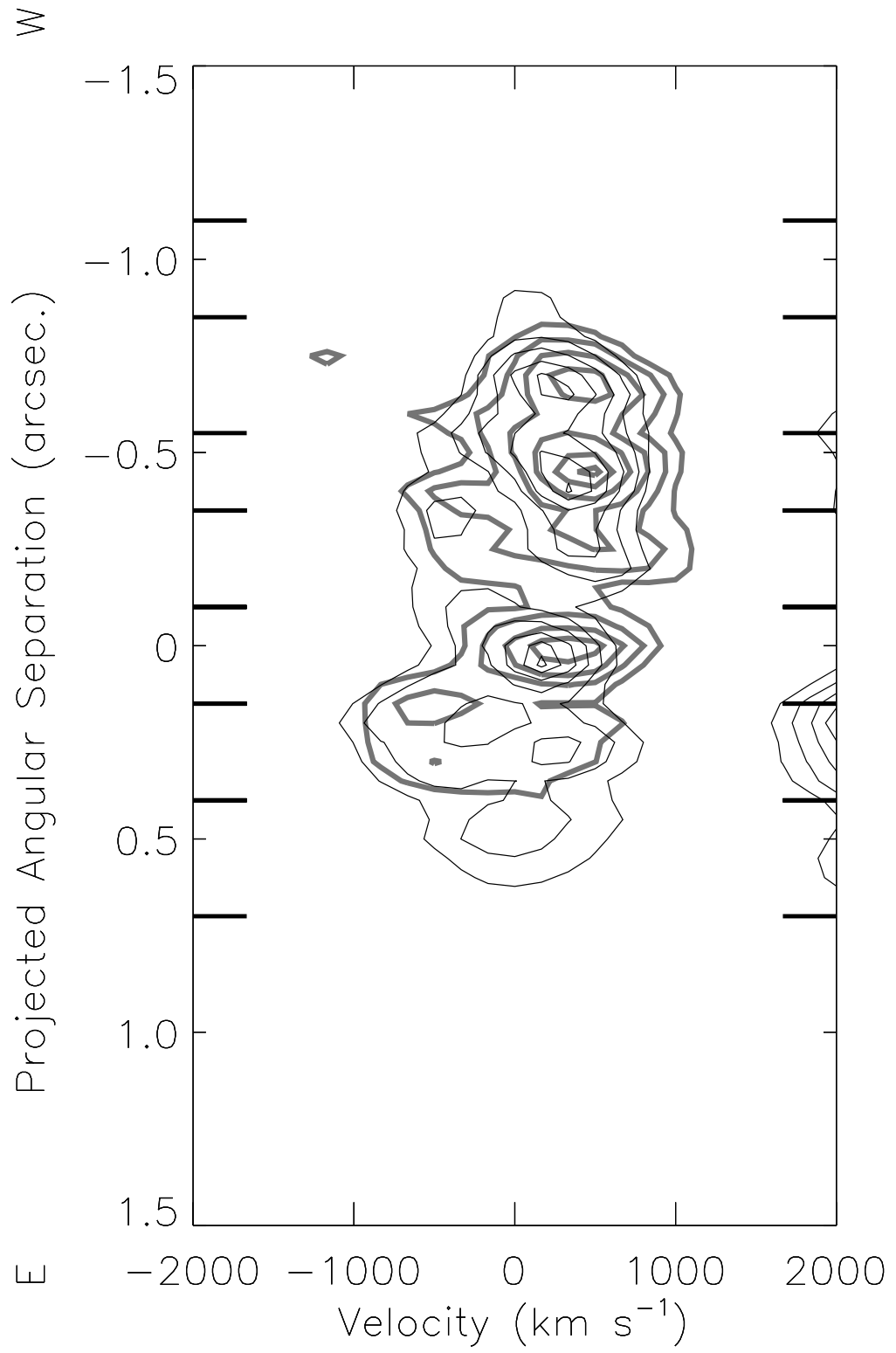


Fig. 2.

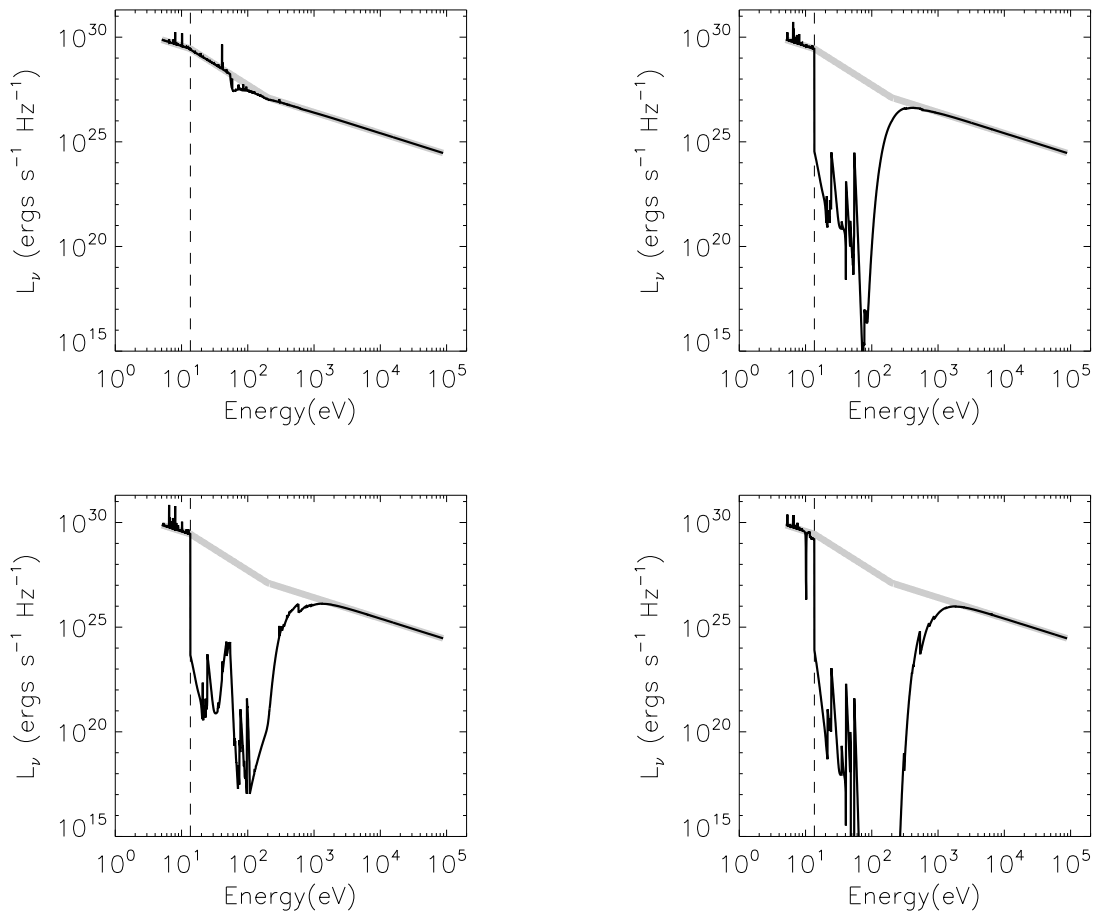


Fig. 3.

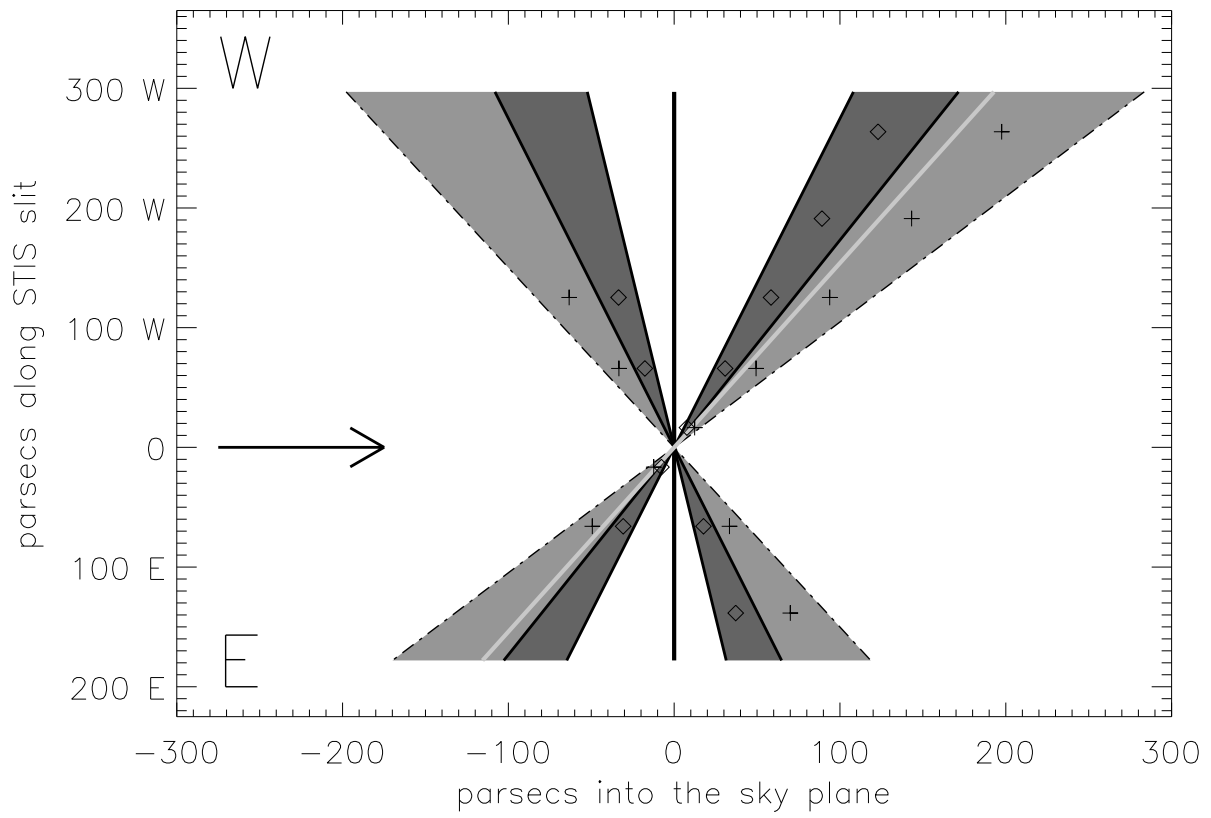


Fig. 4.

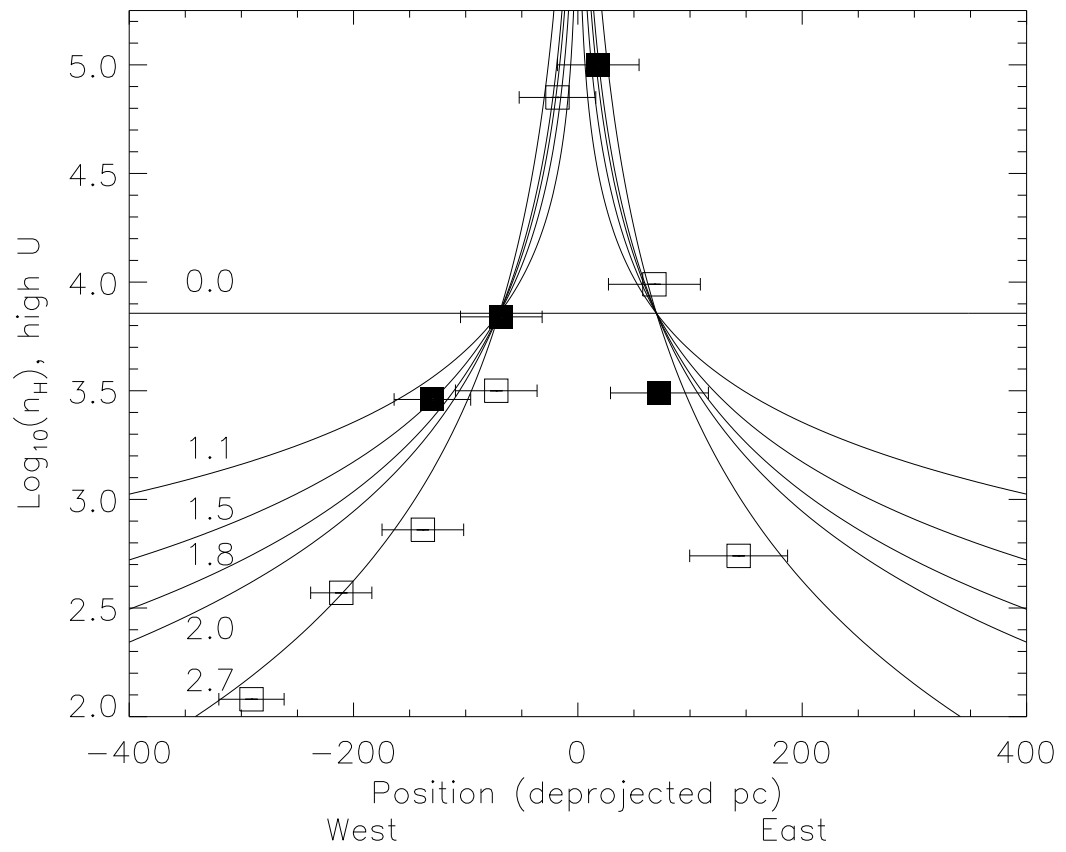


Fig. 5.

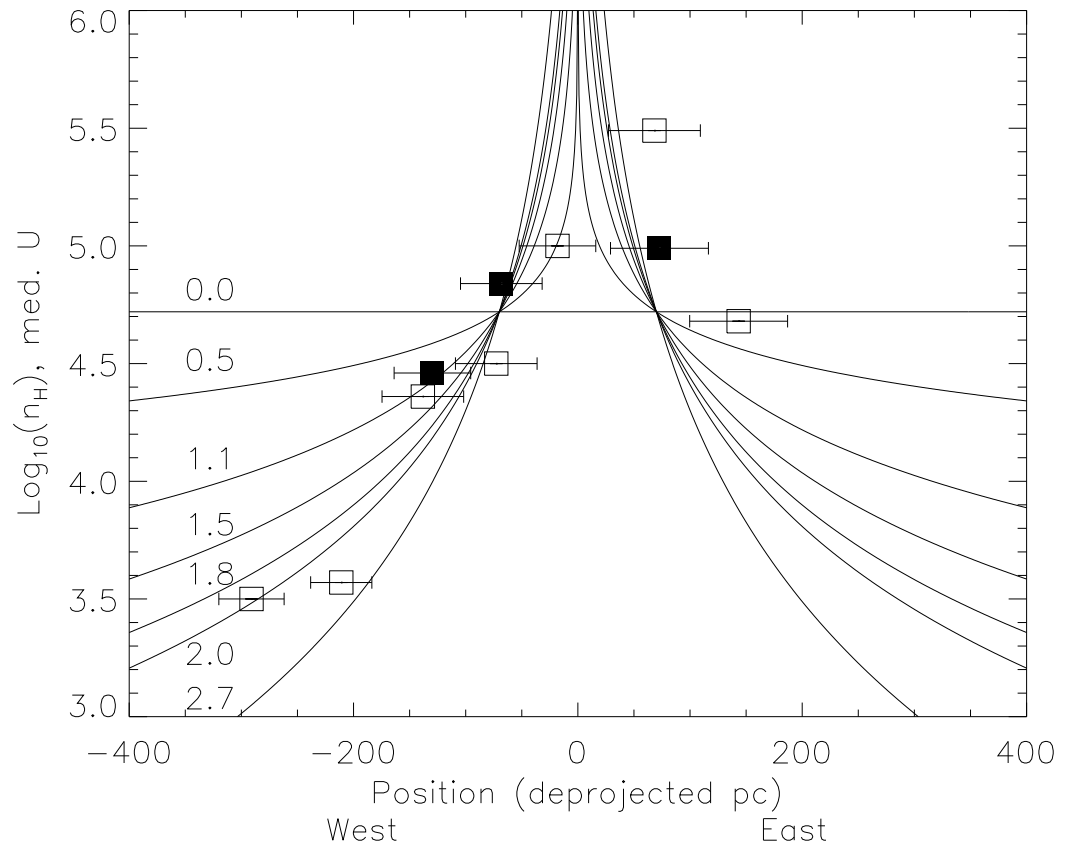


Fig. 6.

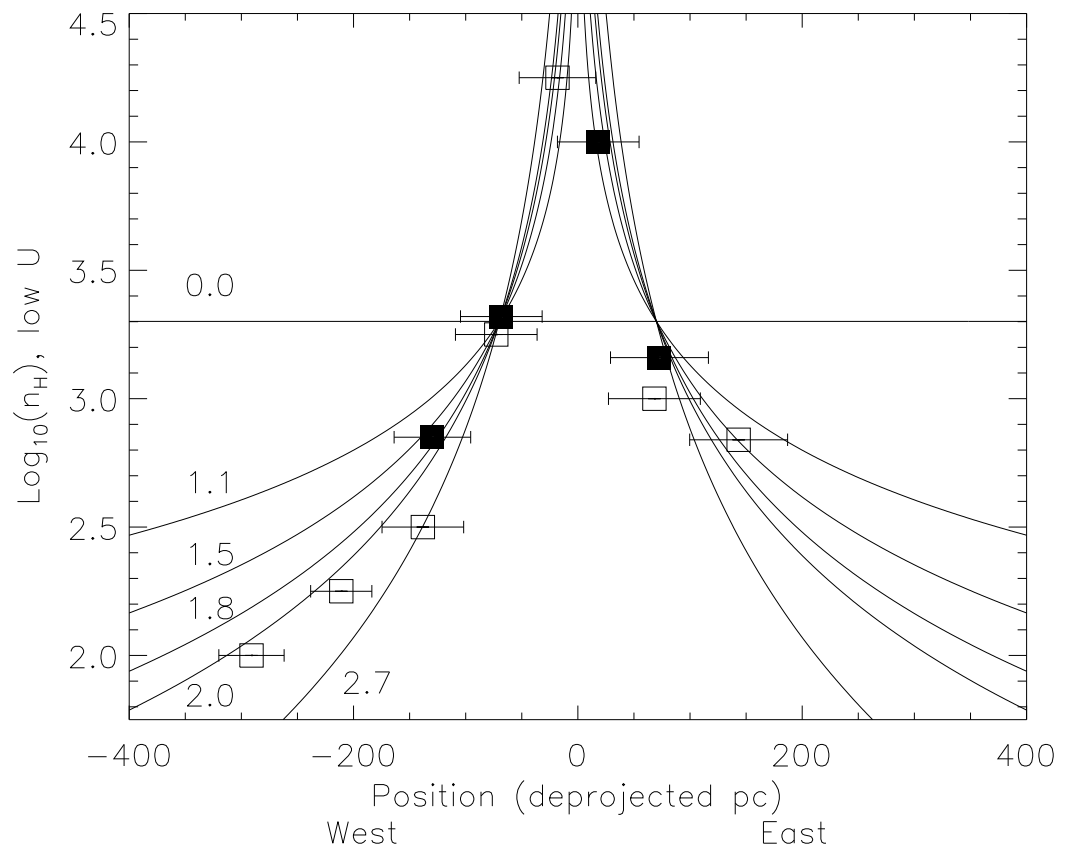


Fig. 7.